STUDY FOR SENSITIVITY FOR $W' \to \tau\nu$ WITH CMS

VON

SÖREN ERDWEG

BACHELORARBEIT IN PHYSIK

VORGELEGT DER

FAKULTÄT FÜR MATHEMATIK, INFORMATIK UND
NATURWISSENSCHAFTEN
DER RWTH AACHEN

IM JULI 2011

ANGEFERTIGT IM

III. PHYSIKALISCHEN INSTITUT A

BEI

PROF. DR. THOMAS HEBBEKER

STUDY FOR SENSITIVITY FOR $W' \to \tau\nu$ WITH CMS

SÖREN ERDWEG

0.1 ABSTRACT

In this bachelor thesis we took a first look at the heavy gauge boson W′ decaying into a tau and tau-neutrino. First we have a detailed look at the W′ and tau decay and its kinematic by studying generator level information of a W′ sample. Secondly we study in detail the leptonic decay modes of the tau into an electron or muon and two neutrinos and at last we have a first look on the hadronic decay modes of the tau, by using hadronic jets and particle-flow taus reconstructed out of hadronic jets. The whole analysis is done with about 900 pb^{-1} of 2011 CMS data.

CONTENTS

0.1 Abstract v

1 INTRODUCTION 1

2 THEORY 2

2.1 Standard Model 2

2.2 Extensions to the Standard Model to additional heavy gauge bosons 4

3 LHC 5

4 CMS 7

4.1 Tracker 8

4.2 Electromagnetic calorimeter 9

4.3 Hadronic calorimeter 9

4.4 Muon system 10

5 GENERAL INFOS ON THE ANALYSIS 11

5.1 Software 11

5.2 Monte Carlo samples 11

5.3 Used quantities 11

5.4 Trigger 13

5.5 Data combination 13

5.6 Statistics 13

6 GENERAL INFOS ON THE TAU'S 15

6.1 Generator level tau decay kinematics 16

6.1.1 Leptonic decay of the tau 16

6.1.2 Hadronic decay of the tau 17

6.1.3 Conclusion 18

6.2 Generator level tau and decay products 18

7 LEPTONIC DECAYING TAU 21

7.1 Data sets 21

7.1.1 Background Monte Carlo samples 21

7.1.2 Signal and data sets 23

7.2 Quality cuts 24

7.2.1 Electron cuts 24

7.2.2 Muon cuts 26

7.3 Kinematic cuts 28

7.4 Results 30

7.5 Conclusion 32

8 HADRONIC DECAYING TAUS 37

8.1 Particle-flow taus 37

8.2 Data sets 38

8.3 Quality cuts 40

8.4 Kinematics 43

8.5 Results 44

8.6 Particle-flow taus 46

9 CONCLUSION 50

I APPENDIX 51

A APPENDIX 53
A.1 Generator level 53
A.2 Kinematic cuts 55
A.3 Monte Carlo samples and Triggers 60
A.4 Electron cuts 63
A.5 Muon cuts 66
A.6 mass limits 70
A.7 Jet cuts 71
A.8 Tau cuts 72

BIBLIOGRAPHY 73
A.9 Acknowledgments 81

1 INTRODUCTION

The W′ is a heavy version of the Standard Model W boson and could solve some problems of the Standard Model by introducing some extensions to the Model. At the moment the two leptonic channels of the W′ decaying into a electron or muon and a neutrino are studied because they can be reconstructed well, so in these channels a signal would be clearly distinguishable. These channels are good to detect the particles because the electron and muon are stable on their way trough the detector. It is more difficult to study the decay of the W′ into a tau lepton, because the mean life time of the tau is not long enough so it decays before it can cross the detector and can only be reconstructed by its decay particles. In the following analysis we take a look at the tau channel and especially into the decayed charged leptons of the tau $\left(W' \to \tau\overline{\nu_\tau} \to e/\mu + \nu_{e/\mu}\nu_\tau\overline{\nu_\tau}\right)$ and have a first look at the hadronic decay of the tau $(W' \to \tau\overline{\nu_\tau} \to \text{hadrons}+\overline{\nu_\tau})$. We use the other leptonic decay channels of the W′ into electron or muon and the analysis of these channels as guideline for the analysis (compare [24], [21] and [9]). The aim of the analysis is to see if the tau channel can be a worthwhile channel in addition to the other two leptonic channels as a third leptonic channel, or if the tau because of the only indirect detection can not be really useful. For that we use about 900 pb^{-1} of 2011 CMS data.

2

THEORY

2.1 STANDARD MODEL

The Standard Model of particle physics can be described by a quantum field theory which describes the elementary particles and the connecting fundamental interactions. The Standard Model includes three of the four fundamental interactions which are mediated by the exchange of gauge bosons between the particles:

- electromagnetism mediated by photons
- weak interaction mediated by $W^{\pm}$ and Z bosons
- strong interaction mediated by gluons.

The electromagnetism and the weak interaction can be described by the unified elektroweak interaction. The strong interaction is described by the quantum chromodynamics (QCD).

The particles of the Standard Model and some of their properties are shown in figure 2.1.

You can distinguish two different kinds of particles depending on their spin, first the fermions (spin = $\frac{1}{2}$) which form the matter and second the bosons (spin = 1) which mediate the interaction. The fermions themselves consist of the electromagnetic, weak and strong interacting quarks and the only electromagnetic and weak interacting leptons. Both the leptons and quarks can be put into three groups called generations, which mainly differ in their mass. For example electron muon and tau have the same charge the same spin and the same quantum numbers but $m_e < m_\mu < m_\tau$.

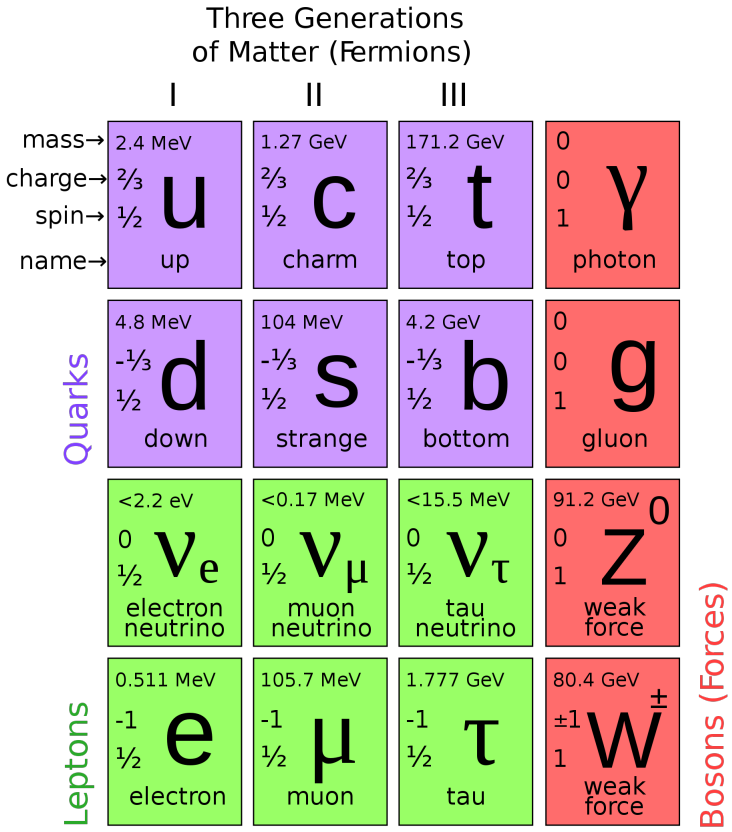

Figure 2.1: Particles of the Standard Model [3]

To each of these matter particles there also exist an antiparticle with exactly the same properties as the particle just the conjugate charge. The bosons mediate the interaction when they are exchanged between two particles. For example in a decay of a neutron a d-quark decays into an u-quark and a W^- and this W^- itself decays into an electron and electron anti-neutrino, resulting in the reaction

$$n \to p^+ + e^- + \bar{\nu}_e.$$

The W boson decays either into a charged lepton and a neutrino (each about 10%) or into hadrons (about 70%). Because of its decay into a charged lepton and neutrino it has the same decay mode as the signal of a W', the main topic of this thesis, and is therefore the main background.

The success of the Standard Model is that it allows a very accurate calculation. It even predicted some of these particles like the bottom quark which which has been found in 1977. This and many other experiments confirmed the Standard Model over a broad spectrum and made it to one of the best understood theories. This and further informations can be found in [16] and references therein.

2.2 EXTENSIONS TO THE STANDARD MODEL TO ADDITIONAL HEAVY GAUGE BOSONS

Even though the Standard Model has many advantages there are still some open issues, because some measured phenomenons are not described by the Standard Model. For example gravitation is not included in the Standard Model. This and other problems may be solved by expanding the model to the Kaluza-Klein theory of extra dimensions [16], to a 'left-right-symmetric' gauge group or other theories. Some extensions, as the two mentioned before, to the Standard Model predict a W′ boson, a heavy particle with charge ± 1 and spin 1. In 1989 Altarelli et al. [17] developed the 'Reference Model' which describes the W′ as a carbon copy of the Standard Model W boson. The 'Reference Model' describes the different decay modes, its branching ratios and cross-sections. The allowed Standard Model W boson decay modes are to decay into a charged lepton and a neutrino $(W \to l\nu_l)$ or into a quark ant-quark pair $(W \to q\overline{q})$. The decay into top and bottom-quark is not allowed because of the higher mass of the quarks. The W′ has the same decay modes, but because of the higher mass of the W′ the decay into top and bottom-quark and the decay into the Standard Model W and Z bosons is allowed. The decay modes in the two bosons is assumed to be suppressed. There is also no interference of the W′ with the Standard Model W. At the moment a W′ is excluded up to a mass of 2.27 TeV by combining the electron and muon channel (comp. [9]).

3

LHC

The Large Hadron Collider (LHC) at the European Organization for Nuclear Research or CERN (Conseil Européen pour la Recherche Nucléaire) in Switzerland and France is at the moment the most powerful particle accelerator in the world. It is build in a tunnel with a circumference of 26.7 km, about 100 m below the surface. Proton or lead ion beams are produced in some pre-accelerators and are accelerated to its final energy and brought to collision at four interaction points (IP). At the moment a center-of-mass energy is 7 TeV. To keep the particles on the orbit there are 1232 superconducting dipole magnets which generate a field of 8.33 T. Additionally there are 4800 magnets of higher order to focus the beams and get them to collide. To keep the magnets superconducting they have to be kept colder than 2 K. In Figure 3.1 the structure and the temperature of the LHC and the experiment caverns are illustrated.

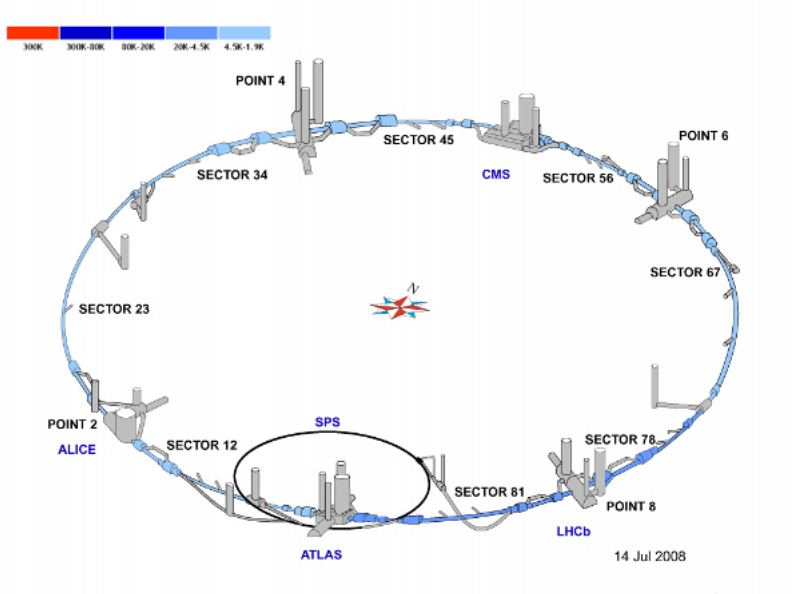

Figure 3.1: LHC layout: Shown is the LHC ring, the experimental caverns for ATLAS, ALICE, CMS and LHCb and also the last pre-accelerator the Super Proton Synchrotron (SPS)[6].

At the four interaction points there are four big experiments to measure the particles coming from the collisions. There are the two multi-purpose detectors ATLAS and CMS whose main task is to search for the Higgs boson, but also for supersymmetry, extra dimensions and other new Physics. LHCb explores, why

the universe consists of mostly of matter and hardly antimatter by studying the decay of B-Mesons and the associated CP violation. The fourth detector ALICE studies the quark-gluon plasma a phase where the quarks are quasi-free, which arises at lead ion collisions. In addition to that there are a few smaller detectors, which share a interaction point with the bigger experiments.

To have a high discovery potential a high event rate is necessary which means we need a high luminosity. In this field the LHC is far better than any particle collider before. The instantaneous design luminosity L is 10^{34} $cm^{-2}s^{-1}$. The expected event number of some process is then

$$N_{event} = \int L dt \cdot \sigma_{event}$$

with σ_{event} being the cross section for the process. Due to this high collision rate the amount of data to be processed locally at CERN is huge. Therefore the Worldwide LHC Computing Grid (WLCG) was built, which can distribute the data to data centers around the world, where they are saved, processed and distributed to the analysts. This and more detailed Information can be found in reference [22].

4

CMS

The Compact Muon Solenoid(CMS) is one of the four big detectors at the LHC and is designed as a general purpose detector for pp and PbPb collisions. The name Compact Muon Solenoid characterizes the main features of the detector, its relative small size, its strong solenoid magnet and its ability to detect muons very well. To detect the many different particles coming from the collisions, CMS is built out of four different sub-detector parts, each with its own task. Closest to the interaction point is the tracker to reconstruct the trajectory of charged particles as close to the interaction point as possible. Next there is the electromagnetic calorimeter to measure the energy of electrons and photons. Outside of the electromagnetic calorimeter comes the hadronic calorimeter to measure the energy of the hadronic particles. All these sub-detectors are inside the Solenoid magnet which generates a homogeneous magnetic field inside the detector of 3.8 T. This field is necessary to measure the momentum of charged particles, by forcing them on a bent trajectory because of the Lorentz force and by measuring the trajectory the momentum can be calculated. The whole detector is divided into three parts, the barrel around the beam pipe and the two endcaps.

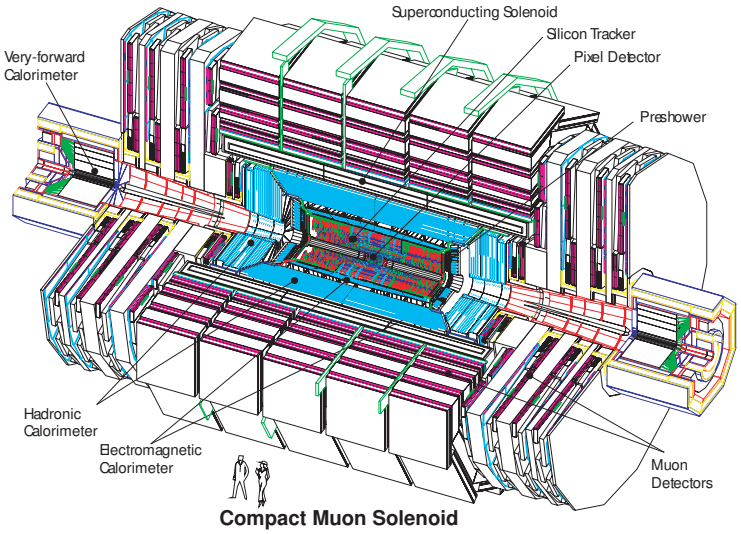

Figure 4.1: complete CMS detector: One can clearly see the positions of the different sub-detectors and also the general layout of the barrel around the beam pipe in the middle and the two endcaps [7].

The most-outer part of the detector is the muon system which is placed inside the iron joke of the magnet. The position of the single sub-detectors is shown in figure 4.1. The function and the structure of these detectors are explained in more detail in the following sections.

To describe the processes in the detector we use a 3 dimensional orthonormal coordinate system with the interaction point as (0,0,0). The z-axis points along the beam axis, the positive x-axis goes from the interaction point to the center of the LHC circle, and the positive y-axis goes upwards. Additionally to that there are the angles φ and η. The azimuthal-angle φ describing the angle in the xy-plane from the positive x-axis and the pseudorapidity η to get a Lorentz invariant form of θ the polar-angle in the yz-plane from the z-axis by the definition $\eta = -\ln\left[\tan\left(\frac{\theta}{2}\right)\right]$. The following informations and more details can be found in reference [15].

4.1 TRACKER

The Tracker consists of two silicon based semiconducting solid state detectors to measure the trajectory of charged particles. First there is the layered pixel detector and two pixel endcap disks on each side which are as close to the interaction point as possible to measure the track and possible secondary vertices as precise as possible (distance to the interaction point 4.4, 7.3 and 10.2 cm). Outside of the pixel detector there is the silicon strip detector that covers a much lager area to get the best possible measurement of charged particles by crossing up to 13 detector layers in the barrel. With an exact measurement of the trajectory we can get the momentum of the particle by the bending of the trajectory in the magnetic field. The position and orientation of the single detector layers can be seen in figure 4.2.

TIB = Tracker Inner Barrel
TID = Tracker Inner Disk
TOB = Tracker Outer Barrel
TEC = Tracker End-Cap.

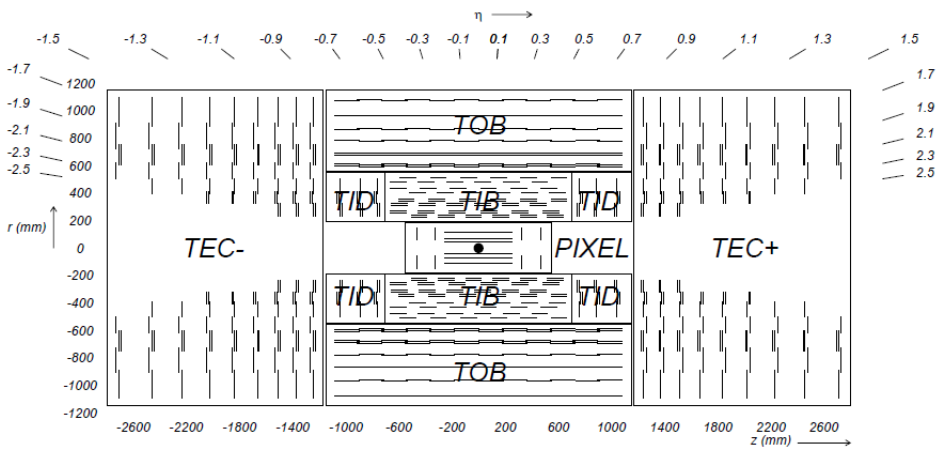

Figure 4.2: CMS tracker: The different detector modules are represented each by a line [15].

4.2 ELECTROMAGNETIC CALORIMETER

Outside of the tracker there is the electromagnetic calorimeter (Ecal) to measure the energy of electrons and photons using lead tungstate crystals in which the electron or photon generates scintillation light. This light is then detected by photodetectors and is translated into the energy amount of the particle. A sketch of the Ecal is shown in figure 4.3. Avalanche photodiodes are used as photodetectors in the barrel and vacuum photo triodes in the endcaps.

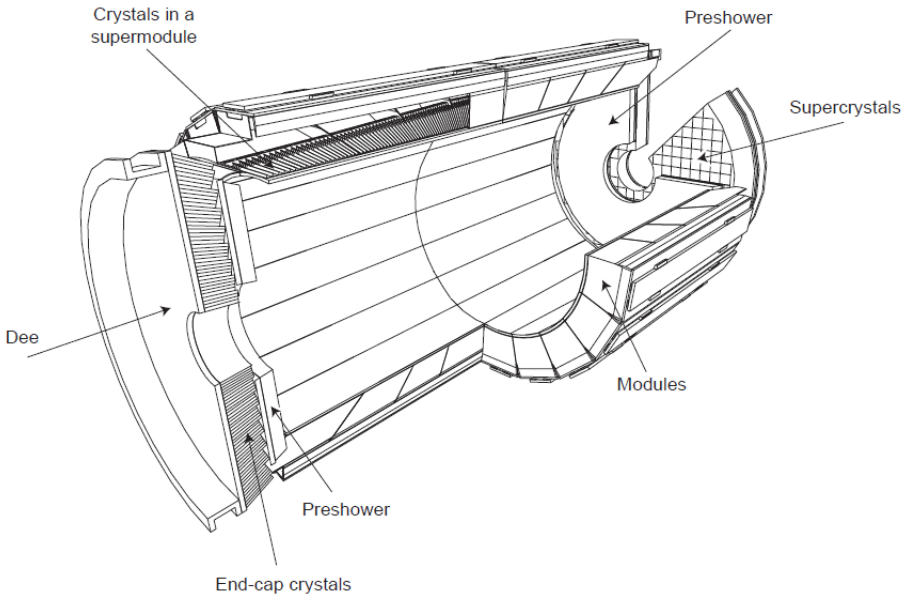

Figure 4.3: CMS Ecal [15]

To detect early decaying particles, in front of the Ecal endcaps the so called preshower detector is installed. It consists of a lead plate and a silicon strip detector behind it.

4.3 HADRONIC CALORIMETER

The hadronic calorimeter (Hcal) of CMS is composed of alternating layers of brass and scintillator and detects hadronic particles via the strong interaction and passing the tracker and the Ecal. The brass layers get the particles to shower and spreading the energy. These resulting particles can then be detected with the scintillates. To measure leakage from the Hcal there is the Hadron Outer (HO) on the outside of the solenoid coil so that in the barrel the minimum absorber depth is 11.8 interaction lengths. To maximize acceptance in the forward direction the Hadron Forward (HF) detector, which covers a $|\eta|$ zone from 3 to 5.2, is placed outside of the muon system. The structure of the barrel and endcap part of the Hcal is shown in figure 4.4.

HB = Hadron Barrel
HE = Hadron Endcap
HO = Hadron Outer
HF = Hadron Forward
Pink = Muon System

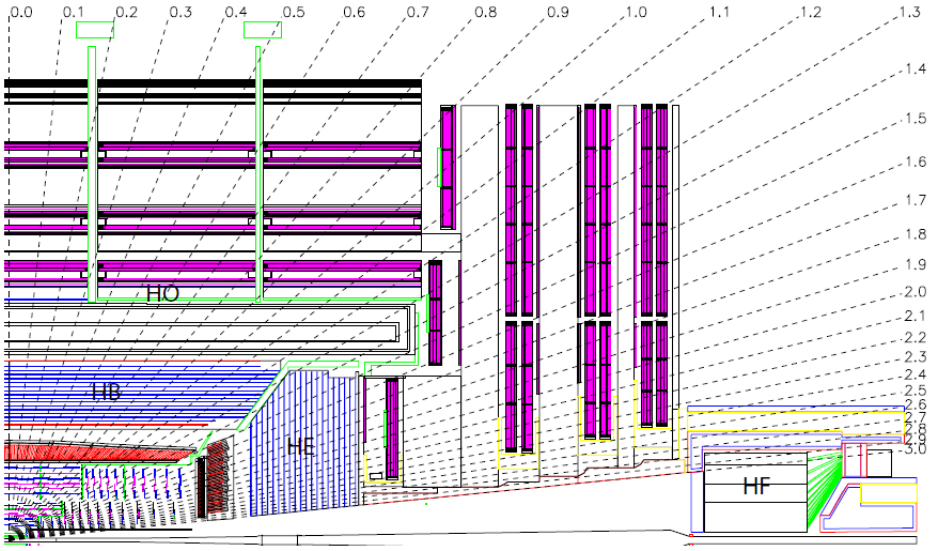

Figure 4.4: Hcal + Muon[15]

4.4 MUON SYSTEM

The muon system of CMS is placed within the iron joke of the magnet, because muons are the only particle which cross the whole detector and can be detected in the muon system. The position of the muon system can be seen in figure 4.4. To get the best possible measurement three detector types are used in the muon system, drift chambers in the barrel and cathode strip chambers in the endcaps where the magnetic field is non-uniform and the particle flux is high. Additionally to that resistive plate chambers are used to get a good time resolution. Neutrinos that also cross the detecter are not detected in any sub-detector they can only be reconstructed as missing transverse energy (see section 5.3)

5 GENERAL INFOS ON THE ANALYSIS

In this chapter the tools which are used in all channels are briefly introduced.

In the whole analysis natural units are used ($\hbar = c = 1$).

5.1 SOFTWARE

For the analysis not the complete data sets are used but a so called skimmed version. Therefore the needed informations of the full data set are taken and written to flat root tuples for further analysis by the skimmer. The used skimmer is ACSusyAnalysis written by Carsten Magass [23] which is used in version 69 for the electron, muon and hadronic and in the newer version 70 for the new particle-flow tau channel. For the analysis the root data analysis framework from CERN is used [26].

5.2 MONTE CARLO SAMPLES

For the analysis the taken data is compared to a simulated background and signal. For that a Monte Carlo generator generates events with the needed background or signal reactions. These events then go trough a full detector and trigger simulation to have set of generator events as detaillike as possible. The used generators are PYTHIA [14], Madgraph [1] and POWHEG [13]. All samples are produced at leading order (LO) and the next-to-next-to-leading order (NNLO) cross-section is calculated by a k-factor. For all calculations the NNLO cross-section is used, with two exceptions that are marked in the sample table.

5.3 USED QUANTITIES

In this section the quantities that are used later on are briefly explained.

- E_T
  E_T is the energy perpendicular to the beam axis, it is defined by $E_T = E \cdot \sin\theta$ and is a conserved quantity.
- $\not{E}_T$
  The missing transverse energy $\not{E}_T$ represents all not measured particles, mainly neutrinos. The neutrinos just leave the detector, but we know that the momentum and energy perpendicular to the beam axis must be zero, because it

was zero before the collision with the conservation of momentum it must be zero afterwards. So we can sum up vectorially all transverse energy components of all reconstructed particles and the difference to zero is the missing transverse energy representing the not measured neutrino. We can not do the same for the energy parallel to the beam axis because the z-component of the colliding particles is not zero.

- M_T
  The transverse mass M_T is defined by

$$M_T = \sqrt{2 \cdot E_T \cdot \not{E}_T \cdot (1 - \cos \Delta\varphi)} \tag{5.1}$$

  where $\Delta\varphi$ is the angle between E_T and $\not{E}_T$.

- particle-flow
  Particle-flow describes a method of reconstructing an event. It uses the informations from all CMS sub-detectors to reconstruct all stable particles and reconstruct out of them the other particles like taus or the missing transverse energy (comp. [8]).

- jet
  Because quarks and gluons can not exist in a free form, they hadronize into hadrons when they are produced in a event (QCD confinement). The trajectories of these hadrons are collimated, so they fly close together called a jet. The jets used for the analysis are calorimeter jets, reconstructed out of the calorimeter informations.

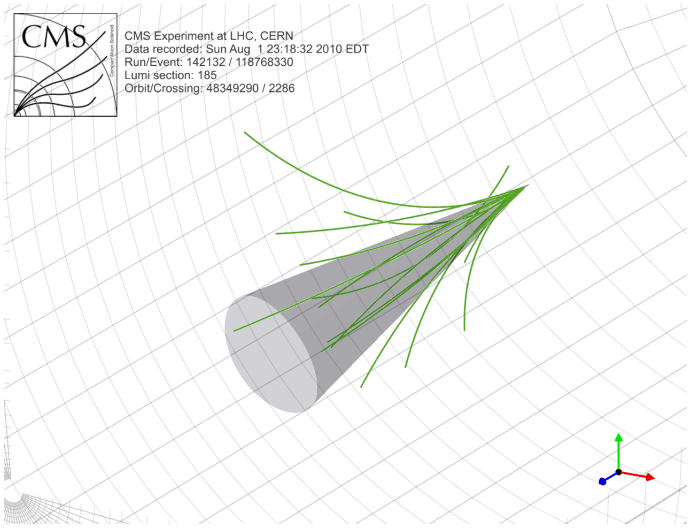

Figure 5.1: Jet: Shown are the different tracks of the measured charged particles and the jet-cone describing the jet [10].

- leptons
  As charged leptons global muons and particle-flow electrons are used. The electrons are reconstructed by the particle-flow algorithm (see above) and the muons are reconstructed out of informations from the muon system together with the tracker.

5.4 TRIGGER

To reduce the huge amount of data produced by CMS because of the high collision rate, a trigger system is used. The trigger uses the detector output to select events that maybe interesting for further studies (e.g the HLT_Mu24 trigger fires if a muon with $E_T > 24$ GeV is in the event).

5.5 DATA COMBINATION

We want to scale the background to the data and they have a fixed number of generated events. For that we use the following relation between the number of expected events, the integrated luminosity and the cross-section

$$N = \int L dt \cdot \sigma. \tag{5.2}$$

So we get a normalization factor w from the number of expected events N and the number of generated events N_{events}, the number of generated events is given for all samples in the sample tables

$$w = \frac{N}{N_{events}}. \tag{5.3}$$

With these two equations we get our normalization factor

$$w = \frac{\int L dt \cdot \sigma}{N_{events}}. \tag{5.4}$$

With this factor we can scale all backgrounds to the integrated luminosity of the data and summarize them.

5.6 STATISTICS

For the statistical analysis to calculate a mass limit of the W′ we use bayesian statistics in a counting experiment implemented in the RooStats95 tool [18]. In that the likelihood function L defined by

$$L = p\left(N|\mu\right) \cdot p_{LN}\left(\nu_{SIG}|\delta_{SIG}\right) \cdot p_{LN}\left(\mu_{BG}|\delta_{BG}\right) \tag{5.5}$$

is used. The p_{LN} are probability density functions (pdf) describing the systematic uncertainties on the signal (SIG) and background (BG). ν is a nuisance parameter describing systematic uncertainties and δ is the relative uncertainty on ν. The used pdf´s are lognormal pdf´s :

$$p_{LN}(\nu|\delta) = \frac{1}{\sqrt{2\cdot\pi}\ln\kappa}\cdot\frac{1}{\nu}\cdot\exp\left(-\frac{\ln(\nu/\hat{\nu})^2}{2\cdot\ln(\kappa)^2}\right) \tag{5.6}$$

with κ defined for signal and background by

$$\kappa_{SIG} = 1+\sqrt{\left(\frac{\Delta L}{L}\right)^2+\left(\frac{\Delta\varepsilon}{\varepsilon}\right)^2} \tag{5.7}$$

$$\kappa_{BG} = 1+\frac{\Delta\mu_{BG}}{\mu_{BG}} \tag{5.8}$$

In there L is the integrated luminosity, ε the signal efficiency, μ_{BG} the expected number of background events and Δx the uncertainty on x. The signal + background event count is assumed to follow a poisson probability

$$p(n|\mu) = \frac{\mu^n\cdot e^{-\mu}}{n!} \tag{5.9}$$

with μ being the number of events:

$$\mu(\sigma, L, \varepsilon, \mu_{BG}, \nu_{SIG}) = \sigma\cdot L\cdot\varepsilon\cdot\nu_{SIG}+\mu_{BG} \tag{5.10}$$

By maximizing the likelihood function we can calculate an upper limit on the signal cross-section σ. For that the observed data, Monte Carlo and signal events are used, if we instead of the data events use random data events diced from the expected background and do this very often we can calculate an expected upper limit and error on this cross-section. This together with the theoretical predicted cross-section is shown in the limit plots. The shown uncertainties on the theoretical cross-section are parton-density-function uncertainties. The parton-density-functions describe the distribution and the momentum of the quarks in the protons, and due to different sets of parton-density-functions follows the uncertainty on the cross-section. The intersection of the theoretical and observed cross-section is the point with the maximum observed and excluded W' mass with a confidence interval of 95%. The event numbers for data, Monte Carlos and signal samples and their uncertainties are determined by integration over the high M_T area where the high signal to background ratio is highest (the 'search window').

6

GENERAL INFOS ON THE TAU'S

In this chapter a short introduction to the searched reaction and its important properties is given.

The difficulty in the analysis of the tau channel is that unlike the electron or muon channel the tau has a mean life time of $(290.6 \pm 1.0) \cdot 10^{-15}$ s (comp. [16]) and therefore decays inside the detector and is detected by its decay products. The complete decay chain is shown in figure 6.1.

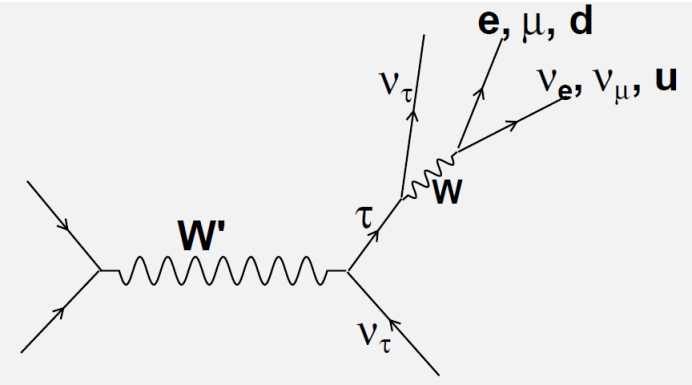

Figure 6.1: complete decay chain

The Feynman graph for the relevant decay of the tau is shown in figure 6.2, with the branching ratios in table 6.1. Everything works exactly the same for the anti-tau, every particle just has to be replaced with its anti-particle.

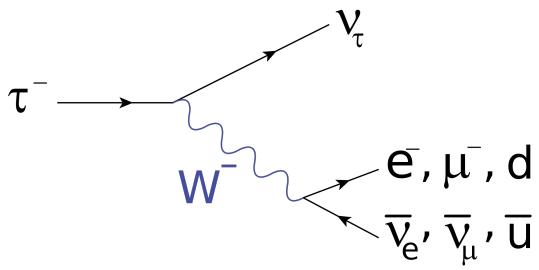

Figure 6.2: τ decay Feynman graph

decay mode	branching ratio [%]
$\tau^- \to \mu^- \bar{\nu}_\mu \nu_\tau$	17.36 ± 0.05
$\tau^- \to e^- \bar{\nu}_e \nu_\tau$	17.85 ± 0.05
$\tau^- \to \mathrm{hadron(s)}$	~ 64

Table 6.1: τ decay modes and branching ratios [16]

6.1 GENERATOR LEVEL TAU DECAY KINEMATICS

Because the tau decay is a three body decay, the first step is to take a look at the decay kinematics. The decay of $W' \to \tau\nu_\tau$ has the same characteristics as the two body decay $W' \to e/\mu + \nu_{e/\mu}$. For the kinematics that means that the angle $\Delta\varphi$ between the lepton (e or μ) and $\not{E}_T(\nu)$ is equal to π and the ratio of E_T^{lep} and $\not{E}_T$ is equal to one. But the tau is only detected by its decay products and the $\not{E}_T$ does not consist only of the ν of the W' decay, so these particles do not have to fulfill these relations. To check this the generator information of a $W' \to \tau\nu$ sample were used to check the relations. First we checked the leptonic decay modes and second the hadronic ones. For this a W' sample with a mass of 1500 GeV is used.

6.1.1 *Leptonic decay of the tau*

The only available information in the skimmer are the information on all leptons but not the connection between them. So the first step is to match the reconstructed leptons to the generated tau by comparing the direction and energy of the tau with all leptons flying in a similar direction with a similar energy. The best matching lepton was selected for the further analysis.

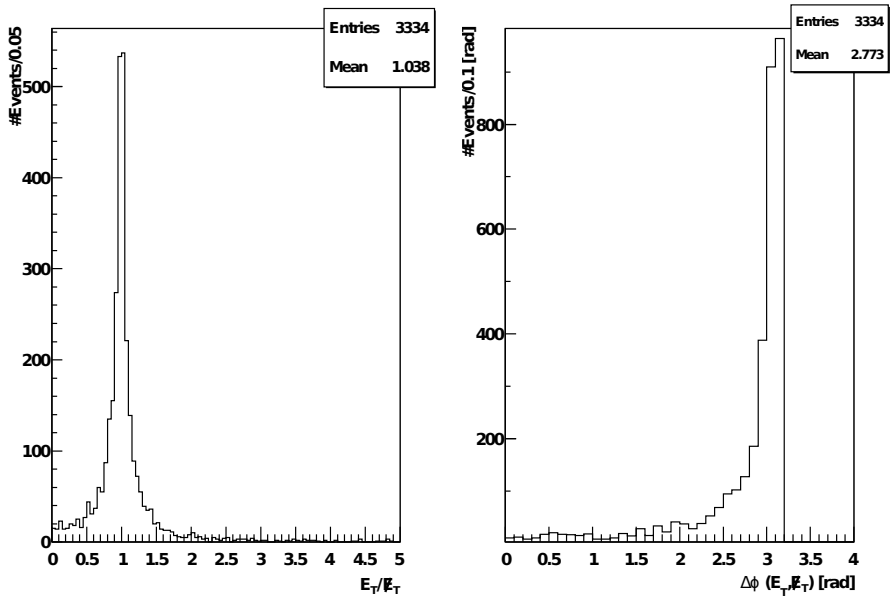

Figure 6.3: Kinematics of the leptonic tau decay: Here is shown the $E_T/\not{E}_T$ ratio and $\Delta\varphi$ for the final state lepton (e or μ) and the missing transverse energy calculated out of the three neutrinos.

With this method we found about 18% of all processes decaying each in an electron or muon. This value matches the theoretical value in table 6.1.

The next step is to calculate an $\not{E}_T$ vector out of the three neutrinos in the event. From this vector we got $\varphi_{\not{E}_T}$ and $\not{E}_T$ to compare it with the values from the lepton and calculate $\Delta\varphi$ and the ratio $E_T/\not{E}_T$ with the results that can be seen in figure 6.3, where we see that the $E_T/\not{E}_T$ ratio is about one and $\Delta\varphi$ is about π as in the $W' \to e\nu$ and $W' \to \mu\nu$ channels.

6.1.2 *Hadronic decay of the tau*

For the hadronic channel we chose events with no matching electron or muon and then we made the same comparison as in the leptonic channel but between the tau and the generated hadronic jets. Also the same way as in the leptonic channel we got an $\not{E}_T$ vector out of the two neutrinos and calculated the relevant values. The results of the calculations for $\Delta\varphi$ and $E_T/\not{E}_T$ are shown in figure 6.4.

pileup: Pileup means that more than one collision is reconstructed as one.
underlying events: Only two quarks collide and produce the searched W′ the others also interact and produce underlying events.

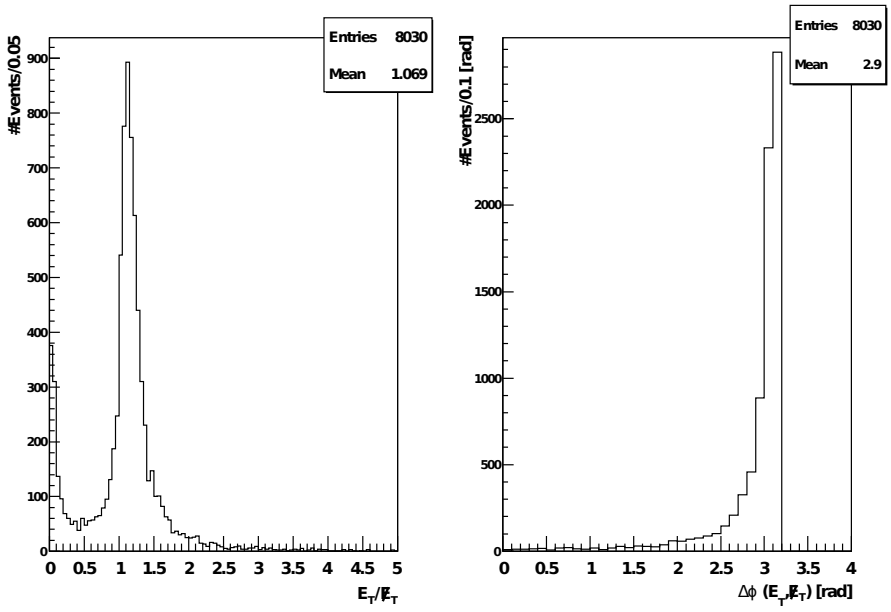

Figure 6.4: Kinematics hadronic tau decay: $E_T/\not{E}_T$ ratio and $\Delta\varphi$ for the hadronic jet and missing transverse energy calculated out of the two neutrinos, as for the leptonic decaying tau we see that $\Delta\varphi$ is about π and $E_T/\not{E}_T$ is about one. The peak in the lower region of $E_T/\not{E}_T$ can be explained by pileup or underlying events.

6.1.3 *Conclusion*

As a summary we can say that the kinematic behavior of the tau decay products is very similar to the electron or muon decay modes of the W′. This result can be explained by the big boost the tau decay products (e.g. $e\ \nu_e\overline{\nu_\tau}$) get from the tau so they fly in the same direction. If you add the two neutrinos vectorially to the one produced in the W′ decay one gets a $\not{E}_T$ vector which has the similar properties as compared to the electron. The same is true for the muon and hadronic channel.

6.2 GENERATOR LEVEL TAU AND DECAY PRODUCTS

The main problem of the tau channel is, that the detected particles as the electron or muon do not have the same energy distribution as the tau itself. To take a look at this problem we made an E_T plot for the tau coming of the W′ and the decayed particles of the tau by using the generator level information on these particles. The different distribution for the tau and the charged lepton are shown in figure 6.5.

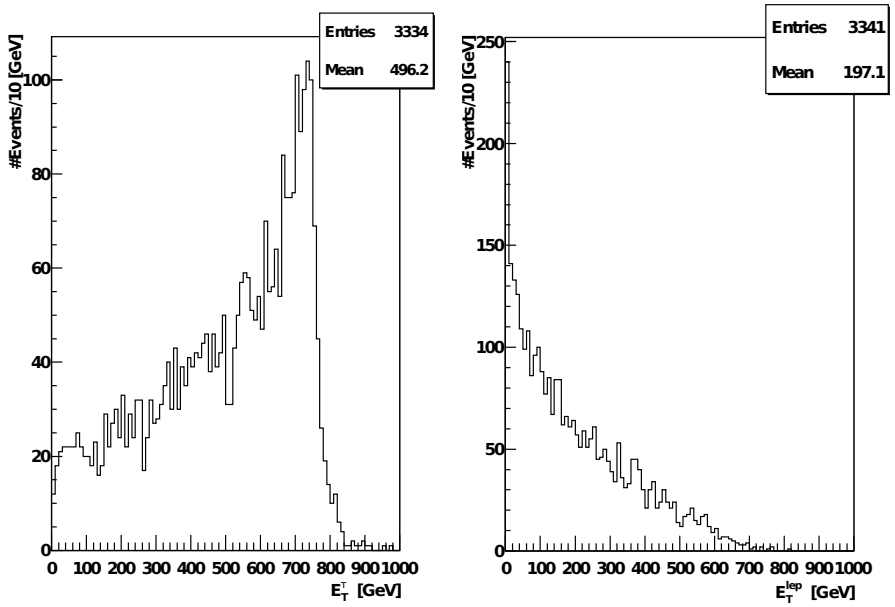

Figure 6.5: E_T^{τ} vs. E_T^{lep}: As we can see that the energy of the tau is clearly defined, with a peak at 750 GeV, but the charged leptons that come from the decay of the tau do not have this clear shape anymore, this can be explained by the subsequent decay of the tau which results in a smearing of E_T due to more decay products.

The problem is that the tau decay is a three body decay so that the energy each particle gets is not discrete. Because we can not measure the energy of the two neutrinos we do not know the exact energy that the tau had. So in this decay we are losing information about the original W′. The comparison between the tau and the jets is shown in the appendix (see section A.1). The same problem is there for the missing transverse energy consisting out of the three (two for a hadronic decaying tau) neutrinos and not only the one from the W′ decay, the corresponding plot is shown in the appendix A.1.

In addition we had a look at the transverse mass (see equation 5.1) because it is the main analysis plot (see ref. [9]) and to see what the difference between the tau and the decayed particle is. The comparison between the generated tau and the leptons is shown in figure 6.6, the comparison between the tau and the jets is shown in the appendix (see A.1).

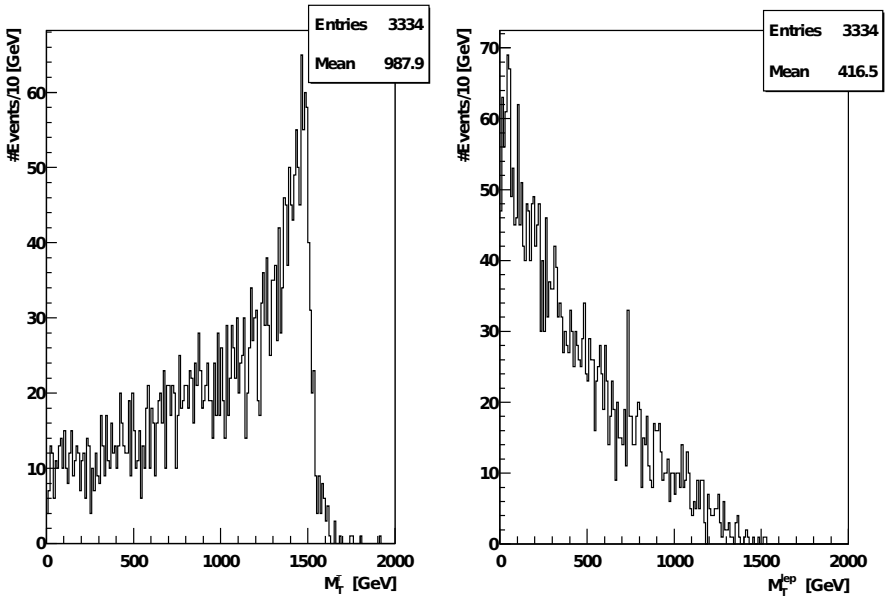

Figure 6.6: Generator level M_T-distribution: M_T^τ vs. M_T^{lep}: In the left plot we see the transverse mass calculated out of the generated tau and neutrino coming directly from the W' and on the right side the transverse mass of the lepton of the tau decay and all three neutrinos is shown.

We can clearly see the Jacobean peak in the left plot from the W' at its mass of 1500 GeV, but the final state leptons and the jets do not have it because in the missing transverse energy there are additional neutrinos, for a hadronic decay one, two for a leptonic decay of the tau, that is not even measured as missing transverse energy itself. The neutrinos can only be measured all together as missing transverse energy, and because the neutrino and tau in the W' decay fly back to back, the neutrinos from the tau decay fly also back to back to the first neutrino because of the boost they get from the tau, but have less energy. So all in all these two neutrinos reduce the energy measured for the lepton (or jet) and also for the missing transverse energy which result in a much lower transverse mass, as seen in figure 6.6. So we see that the measured values (of the final state electron, muon or jet) is not equal to the one of the tau coming from the W'.

7

LEPTONIC DECAYING TAU

In this chapter we take a look at the $W' \to \tau\nu \to e/\mu + \nu_{e/\mu}\nu\nu$ decay. So we are looking for electrons or muons coming from this decay chain.

7.1 DATA SETS

7.1.1 *Background Monte Carlo samples*

For the electrons coming from the decaying taus the same backgrounds as in the $W' \to e\nu$ channel are used. So as background processes all Standard Model processes are used that produce electrons or particles that could be identified as electrons and missing energy from a neutrino or a not reconstructed particle. The background is simulated by a Monte Carlo simulation, the used processes and their important properties are listed in table 7.1. In the appendix a complete list of the used samples is given (see A.1).

- The background with the biggest cross-section is caused by the strong interaction producing multijet events, it is called QCD (for quantum-chromo-dynamics) in the following.

- The most important background is the standard model W boson background because it has the exact same signature as the signal, one lepton and missing energy. Due to that importance two samples for different p_T areas are used to cover the whole signal area.

- In the diboson (WW, WZ and ZZ) and Z/γ (Drell-Yan process) backgrounds arise more than one lepton, so they are only relevant if only one of them is reconstructed within acceptance.

- In the $t\bar{t}$ production the top quark decays into a W boson with the same characteristics as the signal (later labeled as TTJets).

- Last is the γ background when a photon is falsely reconstructed as an electron.

background	generator (p_T binning)	cross-section [pb]	number of events
$W \to e\nu$	PYTHIA ($p_T < 100$)	10438	5076954
$W \to e\nu$	PYTHIA ($p_T > 100$)	1.569	4391900
$W \to \mu\nu$	PYTHIA	10438	5038640
$W \to \tau\nu$	PYTHIA	10438	4753750
$t\bar{t}$	Madgraph (only NLO)	157.5	1164208
QCD (only LO)	PYTHIA($20 < p_T < 30$)	2454400	35336246
	PYTHIA ($30 < p_T < 80$)	3671200	67508892
	PYTHIA($80 < p_T < 170$)	139500	1588698
WZ	PYTHIA	18	2108416
ZZ	PYTHIA	5.9	1745888
WW	PYTHIA	43	1804720
$Drell-Yan$	PYTHIA ($Z \to ee$)	1666	2039987
	PYTHIA ($Z \to \mu\mu$)	1666	2244733
	PYTHIA ($Z \to \tau\tau$)	1666	1977446
$\gamma + Jets$	ALL PYTHIA ($p_T < 15$)	$8.42 \cdot 10^7$	1043460
	($15 < p_T < 30$)	$1.717 \cdot 10^5$	1025840
	($30 < p_T < 50$)	$1.669 \cdot 10^4$	1025480
	($50 < p_T < 80$)	2722	1024608
	($80 < p_T < 120$)	447.2	1048215
	($120 < p_T < 170$)	84.17	1023961
	($170 < p_T < 300$)	22.64	1100000
	($300 < p_T < 470$)	1.493	1098904
	($470 < p_T < 800$)	$1.323 \cdot 10^{-1}$	1093499
	($800 < p_T < 1400$)	$3.481 \cdot 10^{-3}$	1092742
	($1400 < p_T < 1800$)	$1.27 \cdot 10^{-5}$	1097060
	($p_T > 1800$)	$2.936 \cdot 10^{-7}$	1091360

Table 7.1: electron background samples

The used background samples are from the official Monte Carlo production 'Spring 2011' [4].

Similar to the electron channel the same Standard Model backgrounds as in the $W' \to \mu\nu$ channel are used for the muon channel. The used backgrounds are listed in table 7.2. A complete sample list can be found in the appendix (see A.5) in addition also the $W \to \tau\nu$, the diboson, $t\bar{t}$ and two Drell-Yan ($Z \to \mu\mu$ and $Z \to \tau\tau$) samples were used, which were already used in the electron channel and can be found in table 7.1.

background	generator (p_T binning [GeV])	cross-section [pb]	number of events
$W \to \mu\nu$	POWHEG($W^+ \to \mu^+\nu$)	6152	1982936
	POWHEG($W^- \to \mu^-\nu$)	4286	1978590
$W \to \mu\nu$ (high p_T)	PYTHIA ($p_T > 100$)	1.569	4376400
QCD (only LO)	PYTHIA	84679	5000000

Table 7.2: muon background samples

These Monte Carlo samples come as the electron samples from the official 'Spring 2011' production [4].

7.1.2 *Signal and data sets*

Monte Carlo simulations are used for signal simulations of W' with different masses decaying into a tau. The different samples and their properties are listed below in table 7.3.

W' mass [GeV]	cross-section [pb]	number of events
1500	0.0949	11000
2000	0.0135	11000
2200	0.0066	11000
2500	0.0025	11000

Table 7.3: signal samples

The used data sets are listed in table 7.4.

	electron	muon
data set	luminosity [pb^{-1}]	luminosity [pb^{-1}]
rereco 10.05	204.2	204.2
DCS only 17.06	581.5	-
DCS only 24.06	157.6	-
GoldenJSON 27.05	-	682.8
complete used data	943.3	887

Table 7.4: used data sets

DCS only: Data sets for which is checked that the high voltage of the detector is activated.
GoldenJSON: Data sets for which is checked that all detector parts are working correctly.

If we use these background and signal samples for the electrons and plot them together with the data, we get the distributions shown in figure 7.1, the distribution for muons is shown in the appendix (see A.15).

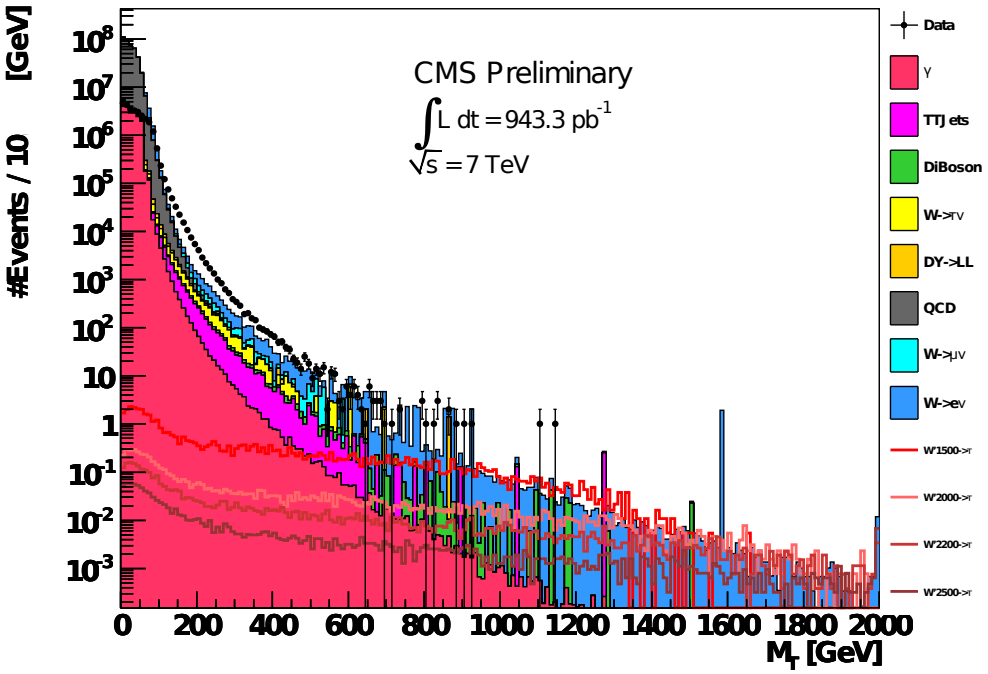

Figure 7.1: Raw data electrons: Shown is the M_T-distribution of the electrons, the difference between data and the Monte Carlo samples is mainly due to different triggers and also different preselection in the skimmer.

To reduce the number of background events and use only well reconstructed events we use some quality cuts, they are briefly explained in the next section.

7.2 QUALITY CUTS

7.2.1 *Electron cuts*

At first we need some quality cuts on data and Monte Carlo samples to isolate high energy electrons. For that the recommendations of the High Energy Electron Positron (HEEP) group in version 3.0, specially developed for this purpose, were used [19]. The cuts are briefly explained in the following. How the cuts work on the different backgrounds can be seen in figure 7.2.

1. $E_T > 35$ GeV
   transverse energy calculated by: $E_T = E \cdot \sin\theta$

2. fired single electron trigger
   the used triggers are listed in table A.4.

3. $|\eta_{SC}| < 1.442$ or $1.560 < |\eta_{SC}| < 2.5$
   to only use particles well measured and exclude the gap

between barrel and endcap (η_{SC}: η measured in the Ecal SuperCluster [comp. figure 4.3])

4. energy measured in Ecal
   electron not only measured in the tracker but in the Ecal

5. $|\Delta\eta| < \begin{cases} 0.005 & \text{barrel} \\ 0.007 & \text{endcap} \end{cases}$
   $\Delta\eta$ between the η measurements in Ecal and tracker

6. $|\Delta\varphi'|<0.09$
   $\Delta\varphi'$ between the φ measurements in Ecal and tracker

7. $H/E < 0.05$
   Hcal energy in $\Delta R = \sqrt{\Delta\eta^2 + \Delta\varphi^2}$ / Ecal energy in SuperCluster

8. $\sigma_{i\eta i\eta} < \begin{cases} n/a & \text{barrel} \\ 0.03 & \text{endcap} \end{cases}$
   $\sigma_{i\eta i\eta}$: Ratio of the energy in the seed crystal (crystal with the highest energy) and the surrounding 5x5 crystal cluster

9. $\text{barrel} : \begin{cases} |\frac{E^{2x5}}{E^{5x5}}| > 0.94 \\ \vee |\frac{E^{1x5}}{E^{5x5}}| > 0.83 \end{cases}$
   $E^{a\times b}$: Energy in $a \times b$ crystals

10. $\text{Hcaldepth} < \begin{cases} 2 + 0.03 \cdot E_T^{calo} & \text{barrel} \\ 2.5 + 0.003 \cdot E_T^{calo} \wedge E_T^{calo} > 50\text{GeV} & \text{endcap} \\ \vee 2.5 \wedge E_T^{calo} < 50\text{GeV} & \text{endcap} \end{cases}$
    Hcaldepth1: transversal energy in the Hcal in a cone with the radius 0.3 around the electron position excluding a cone with the radius 0.15

11. $\text{Hcaldepth2} < \begin{cases} n/a & barrel \\ 0.5 & endcap \end{cases}$
    Hcaldepth2: exactly as Hcaldepth1 just other calo towers.

12. Track p_T isolation $< \begin{cases} 7.5 & \text{barrel} \\ 15 & \text{endcap} \end{cases}$
    Track p_T isolation: Sum p_T of all tracks within a ΔR cone between 0.04 and 0.3.

13. single electron in event (not an official HEEP cut)

14. kinematic cuts (see section 7.3)

15. good vertex
    good vertex means that the reconstructed primary vertex fulfills: $|z| < 24$ cm and $\mathrm{Ndof} > 4$.

7.2: cut efficiency compared to the last cut before

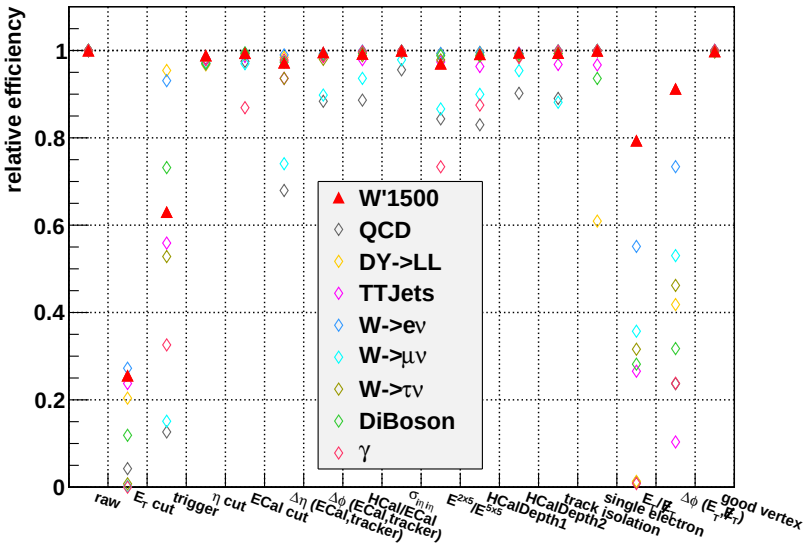

Figure 7.2: cut flow electron for quality + kinematic cuts

The cutflow (figure 7.2) shows the impact of the various selection steps on signal and background. For example in the single electron cut the events with theoretically more than one electron like Drell-Yan or diboson are reduced depending on the number of electrons. The signal is mainly decreased in the first E_T and trigger cuts to the expected about 18% which correspond to the branching ratio $\tau \to e\nu\nu$ of 17.9% (see table 6.1). The decrease in the kinematic cuts is because they are optimized for a high signal to background ratio, and not a high number of signal events, they are explained in more detail in the following section. Some of these cuts do not do much on Monte Carlo samples but select the good quality electrons in data.

7.2.2 *Muon cuts*

The quality cuts to isolate high energy muons are explained next. The cuts base on the recommendation of the muon physics object group for high p_T muons [25] and are listed below. The cutflow for the different samples is shown in 7.3.

1. fired single muon trigger and $p_T > 25$ GeV
   the used triggers are listed in table A.4.

2. must be tracker + global muon
   which means the muons must be detected by the tracker and the muon system.

3. at least 11 hits in the tracker
4. at least 1 hit in the pixel detector
5. at least 1 hit in the muon detector
6. a χ^2/Ndof < 10 for the global track
   The χ^2/Ndof is calculated for the reconstructed muon track, so that only well reconstructed muons are selected.
7. transverse impact parameter with respect to the beam spot <0.02 cm
   The impact parameter is the distance between the origin of the muon and the beam collision point, with that cut cosmic muons can be reduced (the cut is a factor 10 tighter than in the recommendation, to reduce non-prompt muons).
8. at least 2 matched muon segments
9. $|\eta| < 2.1$
10. only one global muon
11. relative track isolation <0.1
    The relative track isolation is defined as the sum of p_T of all tracks in a cone with $\Delta R < 0.3$.

The efficiency of the different cuts plus the kinematic cuts is shown in the following cut flow 7.3:

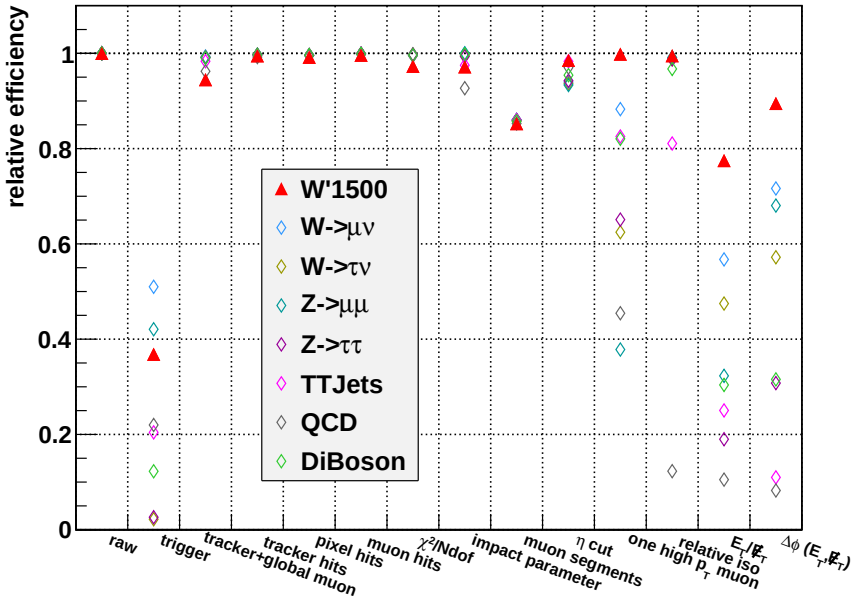

Figure 7.3: cut flow muon quality and kinematic cuts

In this cutflow, as in the electron channel, we see that the signal is mostly reduced by the trigger to the expected value around

18% corresponding to the branching ratio. The deduction in the kinematic cuts is also because of the optimization on signal to background ratio and not on absolute signal events. The first cuts select the good reconstructed muons out of data and do not much on the Monte Carlo samples because they contain only good reconstructed muons.

7.3 KINEMATIC CUTS

Now we have good reconstructed electrons and muons, but we also need a high signal to background ratio to make sure a potential signal would be visible. For that we use the kinematic behavior of the W' decay and the final state leptons on $\Delta\varphi$ and the ratio $E_T/\not{E}_T$. We know that the expected value is $\Delta\varphi = \pi$ and $E_T/\not{E}_T = 1$ from section 6.1, so the question remains how to cut around this values. To get the best possible values for the upper and lower cut value on the $E_T/\not{E}_T$ cut and the lower cut value on the $\Delta\varphi$ cut for each of this cuts the cut value was varied and the number of events counted which survive this cut.

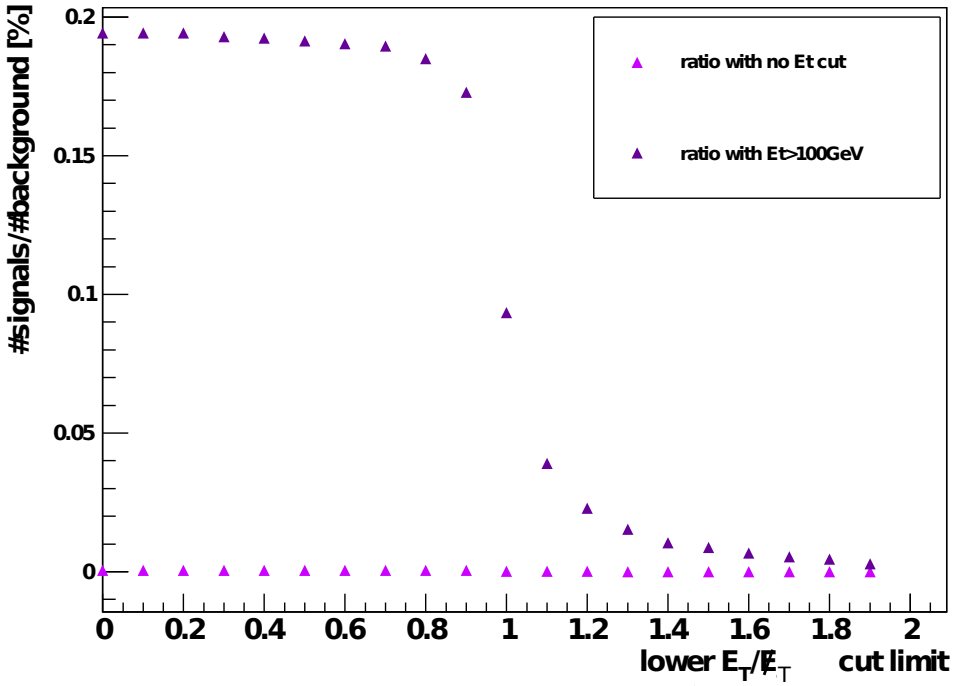

Figure 7.4: Electron lower $E_T/\not{E}_T$ cut

For the different values out of the surviving event numbers the efficiency for this value was calculated, additionally to that the signal over background ratio, because it indicates how good we can see a signal, and the signal over square root of background ratios, which indicates how significant the signal would be, were

calculated. The resulting signal to background ratio for the lower $E_T/\not{E}_T$ cut value in the electron channel is shown in figure 7.4. The efficiencies, the signal over square-root of background ratio and the plots for the muons are shown in the appendix (see A.2).

For the lower $E_T/\not{E}_T$ cut value shown in figure 7.4 the upper cut value was set to 2.1 and the lower was varied from 0 to 1.9 in 0.1 steps. From each of these cuts the number of surviving events were compared to the event number before the cut, to get the corresponding efficiency. To get a better comparison between signal and background the backgrounds were summarized. As we can see in the plot the signal to background ratio is close to zero because of the high number of background events, so we take a look at the high energy area, where the ratio should be much better (see figure 7.1). For that before the $E_T/\not{E}_T$ cut a $E_T > 100$ GeV cut was implemented and then the same procedure as before was performed. As we can see in the plots the results with this cut are much better, and we can definitely see some cut values in the shape of the distribution. As the cut value the first point was chosen were the signal over background ratio changes non-linear. The signal to background ratios are very small even with the E_T cut, but for a higher cut-value the shape of the distributions does not change only the ratio. Due to the higher statistics, because we take more events into account, the cut on E_T was not changed.

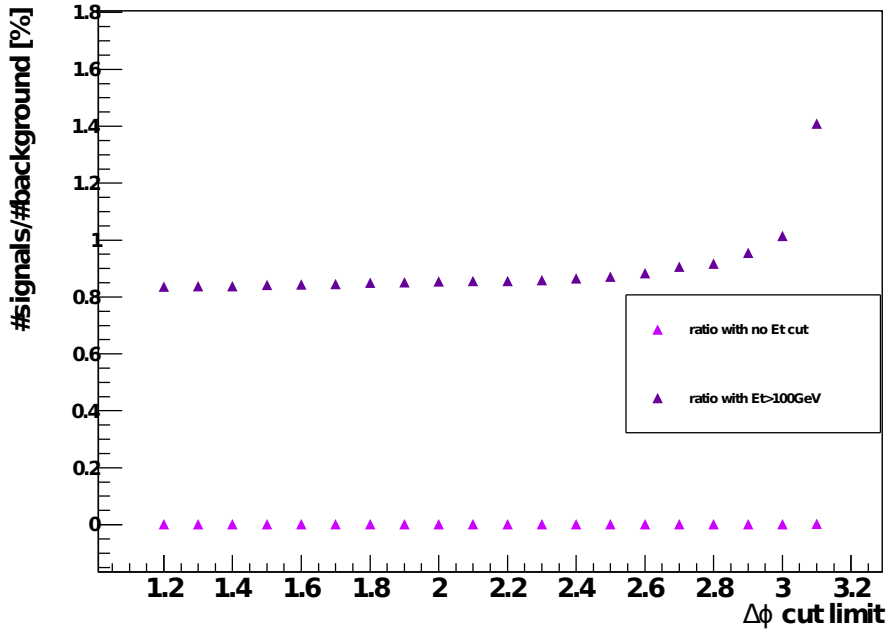

Figure 7.5: Electron $\Delta\varphi$ cut

For the $\Delta\varphi$ cut we know that the expected value would be π so we varied the lower cut value on $\Delta\varphi$ and set no upper cut value. The cut value was varied from 1.2 to 3.1 in 0.1 steps. The signal to background ratio for the electrons is shown in figure 7.5. The efficiencies and the plot for the muons are shown in the appendix (see A.2).

The goal is to get a high signal to background ratio without loosing too much signal. With that we chose the following cut values as a compromise between a high signal to background ratio and a high number of signal events, as the first point that differs from the linear shape of the distribution up to that:

- $E_T/\not{E}_T \begin{cases} < 1.2 \\ > 0.8 \end{cases}$

- $\Delta\varphi > 2.8$

These are the cut values used for the following analysis. Compared to the cut values in the $W' \to \mu\nu$ and $W' \to e\nu$ channel ($0.4 < E_T/\not{E}_T < 1.5$ and $\Delta\varphi > 2.5$) our used cuts are much tighter, to get a good signal to background ratio although the branching ratio is much smaller.

7.4 RESULTS

In a next step these quality and kinematic cuts are applied to the background and signal samples and the data.

The transverse mass (defined in equation 5.1) distribution before all cuts shown at the beginning of this chapter in figure 7.1. After all cuts explained in sections 7.2.1 and 7.3 are applied the distribution shown in figure 7.6 follows, the different stages after each cut are shown in the appendix (see A.4). To make the distributions more clear, in all shown M_T plots the backgrounds are summarized while the signal is shown in the front, the distribution with all different backgrounds stacked can also be found in the appendix (see A.4).

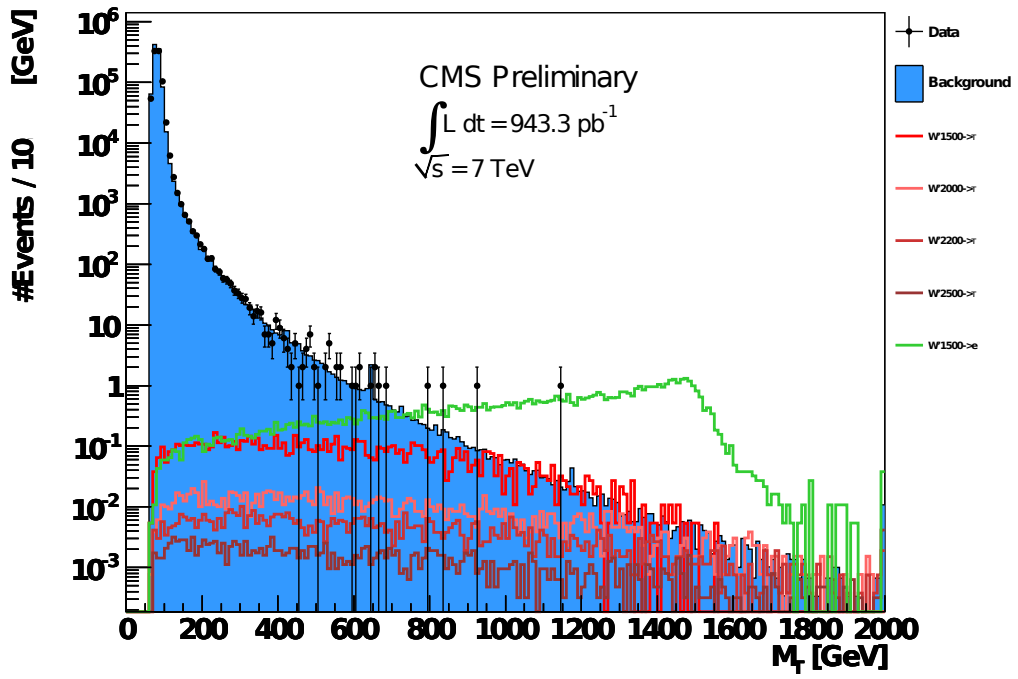

Figure 7.6: Resulting data electrons: One can clearly see the Standard Model W peak in the low M_T region. The signal is evenly distributed as expected from the generator level analysis (comp. 6.6) and has no characteristic peak. For comparison the final M_T-distribution of a $W' \rightarrow e\nu$ sample (green in the plot) with a mass of 1500 GeV with its characteristic Jacobean Peak is shown.

As a comparison the M_T-distribution of the $W' \rightarrow e\nu$ channel is also shown in figure 7.6, where we can see that the signal distribution is not a flat one as for the electron coming from a tau, but has a Jacobean Peak in the high M_T region, and the whole distribution is higher than for the electron coming from the tau, because of the higher branching ratio for that decay.

The final M_T-distribution for the muons coming from the tau decay after the quality and kinematic cuts explained in sections 7.2.2 and 7.3 is shown in figure 7.7, we can see the same signal characteristic as for the electrons.

The agreement between data and Monte Carlo samples can be seen at the η and E_T distributions, they are shown for the electrons and muons in the appendix (see figure A.13 for electrons and figure A.19 for muons).

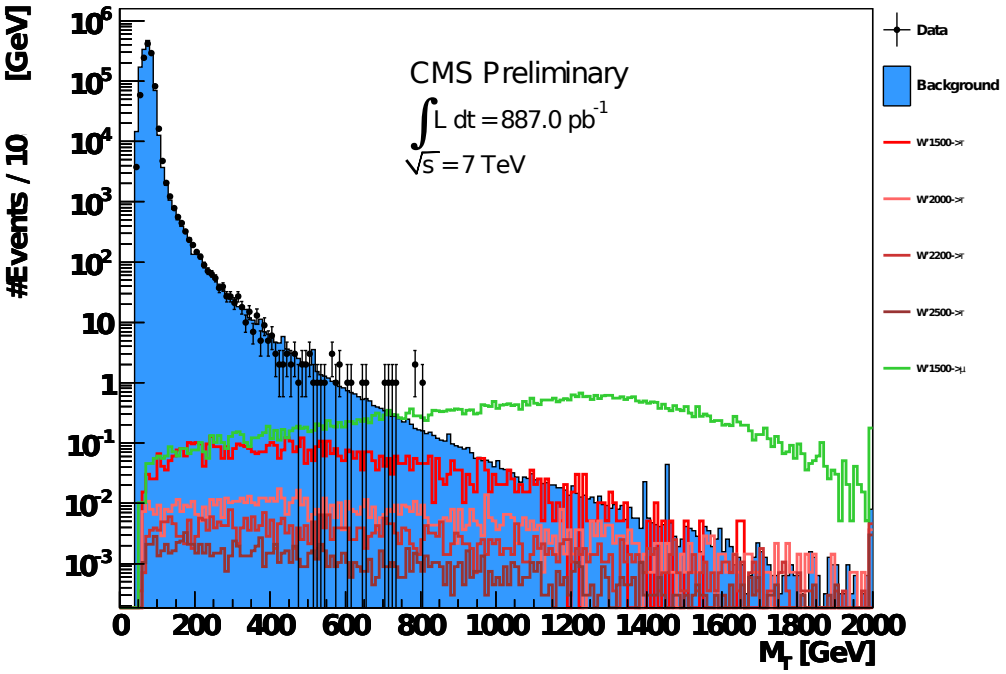

Figure 7.7: Resulting data muons: As in the electron distribution we can see the Standard Model W peak in the low M_T region and signal is evenly distributed with no characteristic peak an event display of the highest M_T event can be seen in the appendix (see section A.5). As a comparison the final M_T-distribution of a $W' \to \mu\nu$ sample with a mass of 1500 GeV is shown, like for the electrons we see the jacobean peak and the over all bigger signal, because of the higher branching ratio, the difference to the electron channel can be explained by the lower p_T resolution for high p_T-muons.

7.5 CONCLUSION

With this good Monte Carlo data agreement we now want to quantify the results. There are three different ways to do that based on different assumptions:

1. We assume that we can distinguish between charged leptons coming from a tau decay and the one coming directly from the W'.

2. We assume that the decay modes of the W' into the three leptons are not equal, and that the only allowed leptonic decay mode is into tau and neutrino.

3. We assume that we can not distinguish where the lepton origins from.

The first is that we assume that we can distinguish between electrons and muons coming from a tau decay by a reconstructed secondary vertex and electrons and muons coming from a W′ decay which would be difficult because of the short life time of the tau. In that case we want to use the data either to find the W′ or to set an exclusion limit on the W′ mass. As we see no excess in data compared to the Monte Carlo background as expected for a W′ we want to set a mass exclusion limit. To get that we want to get an upper limit on the cross-section excluded by these data set and what that means for the possible W′ mass. For that we make one last cut on M_T. The highest signal to background ratio is obviously in high M_T regions, so we need a compromise between high signal to background ratio and enough events for good statistics.

We optimized the M_T cut value for the best agreement between expected and observed cross-section and cut on $M_T > 300$ GeV. To get a higher resolution for the observed and expected cross-sections not only the four signal samples shown in the M_T-plots, but 17 samples with different masses were used, they are listed in the appendix in table A.3, they have gone through the same cuts as the four samples shown above. How to calculate these observed and expected cross-sections is briefly explained in section 5.6 and the result for the tau decaying into a muon is shown in figure 7.8.

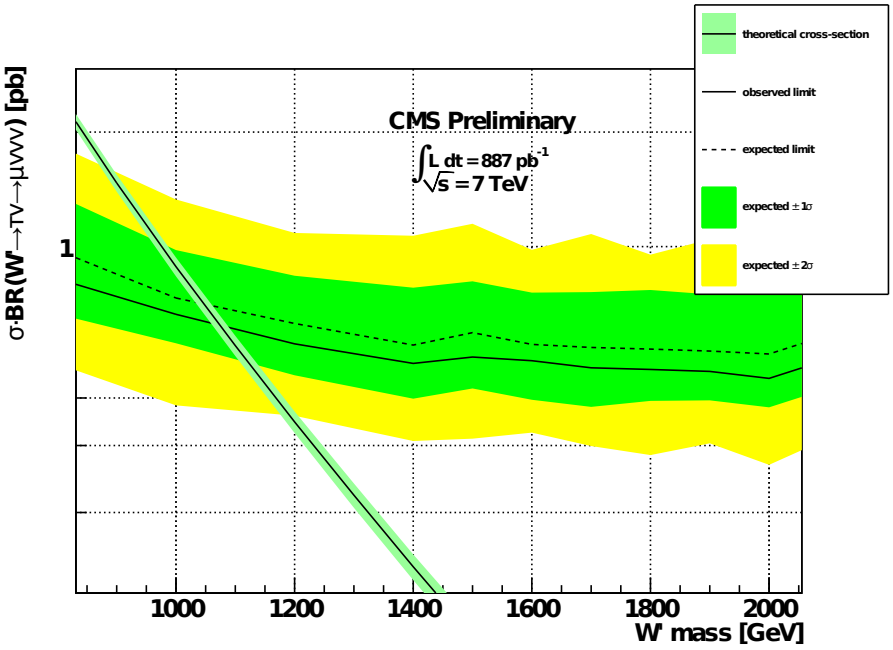

Figure 7.8: Muon limit plot: We can see that the observed cross-section confirms the expected one, and we get an W′ mass limit of $m_{W'} > 1075$ GeV.

Used uncertainties:
- luminosity: 6%
- background events: uncertainty on the integral over the background events
- signal efficiency: Integral uncertainty put forward to the efficiency

more information on the uncertainties can be found in ref. [9].

For the calculation the values and uncertenties listed in table 7.5 were used.

quantity	value	uncertenty
luminosity [pb^{-1}]	887	53.22 (6%)
number of background events	187.2	2.8
number of observed events	182	-
signal efficiency [%] $m_{W'} = 1000$ GeV	4.4	0.2

Table 7.5: Used values and uncertenties for the muon limit calculation.

From this plot we can take an exclusion mass limit for the $W' \to \tau\nu \to \mu\nu\nu$ of 1075 GeV. In order to get an even better exclusion limit we also have to take the $W' \to \tau\nu \to e\nu\nu$ decay into account. The limit plot for this decay is shown in the appendix (see figure A.22).

We have calculated 2 different W′ mass limits for each channel separately. But we can get a better limit by combining the channels.

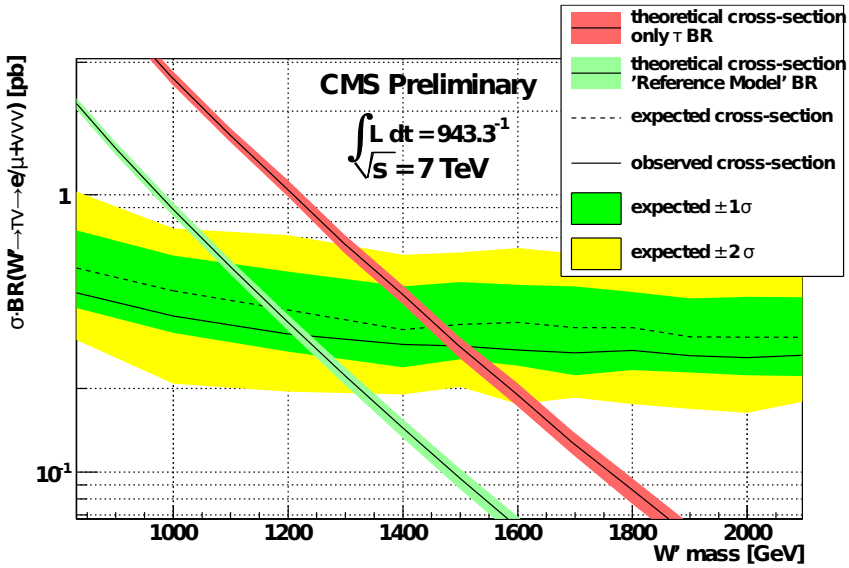

Figure 7.9: Combined limit plot: By combining the limits of the electron and muon we get a mass limit of $m_{W'} > 1150$ GeV from the intersection of observed cross-section and the theoretical one with 'Reference Model' branching ratios. If we assume that the W′ decays leptonically only in taus we get a mass limit of $m_{W'} > 1500$ GeV from the intersection of observed and theoretical cross-section with only τ branching ratio.

By combining the channels the signal efficiency gets higher because we take much more signal events into account. For this calculation the Bayesian Analysis Toolkit were used [11]

which adds the likelihoods used for the single channel limit. The resulting limit plot for the muon and electron of the tau decay are shown together in figure 7.9.

Also shown in this plot is the second purely academic possibility to quantify the results by assuming that the decay modes of the W′ into electron, muon or tau are not equal, and that the decay into a tau and neutrino is the only allowed leptonic decay mode. In that case in the M_T-distributions for electrons (see figure 7.6) and muons (see figure 7.7) would only the signal changed by a factor of three, but because only the signal efficiency is necessary for the limit calculation we have to set a mass exclusion limit, but the theoretical cross-section which was calculated for equal branching ratios for the three leptionic decay modes would increase by a factor of three for the $W' \to \tau\nu$ decay mode.

By combining the electron and muon channel, we get a W′ mass limit of $m_{W'} > 1150$ GeV which can not compete with the limit obtained in the direct decay of the W′ into an electron or muon of $m_{W'} > 2270$ GeV because of the much lower branching ratio and if we assume the different branching ratio of the W′ we can exclude the W′ up to a mass of 1500 GeV.

The third way to quantify the results is to assume that we can not distinguish from where the electron or muon comes from because the tau would only make very few hits in the pixel detector or no at all and together with the single track of the charged lepton a reconstruction of a secondary vertex is not possible.

	$W' \to \tau\nu$ sample ($m_{W'} = 1500$ GeV)	$W' \to \tau\nu$ sample ($m_{W'} = 2000$ GeV)	$W' \to e/\mu\nu$ sample ($m_{W'} = 1500$ GeV)
branching ratio into electrons: 17.85 ± 0.05		branching ratio into muons: 17.36 ± 0.05	
decay into an electron [%]	10.5 (1729 events)	10.9 (1804 events)	72.9 (12025 events)
decay into a muon [%]	7.6 (1251 events)	8.1 (1340 events)	60.0 (9908 events)
decay into an electron [%] with $M_T > 1100$ GeV	0.6 (105 events)	1.8 (291 events)	46.3 (7637 events)
decay into a muon [%] with $M_T > 1100$ GeV	0.4 (66 events)	1.2 (198 events)	37.7 (6223 events)

Table 7.6: Efficiencies of leptonic decaying taus: The event numbers and ratios are calculated from the listed W′ samples and are not scaled.

In that case we take the leptonic decaying tau as an additional signal for the $W' \to e\nu$ and $W' \to \mu\nu$ channels, because we can not distinguish between electrons and muons coming from the decaying tau or direct from the W′. For this the efficiency of the selection is important, how much of the signal gets selected.

Because of the different M_T-distributions as seen in figures 7.6 and 7.7 for leptons from the W′ decay and the leptons from a tau decay, we would see the additional leptons from the tau decay first in the low M_T region, where the difference is largest but for the current analysis of the $W' \to e\nu$ and $W' \to \mu\nu$ channel they are not significant because of the low event numbers.

8

HADRONIC DECAYING TAUS

The hadronic decay of the tau is the decay with the highest branching ratio (see table 6.1), so it is important to have a look into that channel. The hadrons can not be detect each alone, they are detected as many particles together called a jet ($W' \to \tau\nu \to$ hadronisation $\to$ jet). So the first step is to have a good measurement of these jets, next is to distinct between the tau jets and the jets from other sources. To have a first look at the hadronic decay of the tau, the background samples of the electron channel were used. Unfortunately these samples are skimmed on at least one electron. Since the main focus is on the leptonic part there are no extra samples without electron requirement. Many hadronic jets contain electrons, so that we can get some first results. For the analysis of the jets two different methods were chosen, first to have a direct look at the jets and second to have a look at the particle-flow taus, which are reconstructed only out of jets. The algorithm to reconstruct the tau is the shrinking cone algorithm and is briefly explained in the next section.

8.1 PARTICLE-FLOW TAUS

The pf-tau is reconstructed out of all objects with $p_T > 0.5$ GeV in a cone with $\Delta R = \sqrt{(\Delta\varphi)^2 + (\Delta\eta)^2} = 0.15$.

The cone is defined around the leading track (track of the highest p_T particle) in the jet. The jet is reconstructed with the anti$-k_t$ algorithm in a cone with size 0.5 (comp. [5]).

The leading particle must be in a cone with $\Delta R = 0.1$ around the jet and must have a $p_T > 5$ GeV. In addition to that there is the isolation condition, consisting out of two cones, the inner signal cone and the outer isolation cone. Between these two may be no charged hadron with $p_T > 1$ GeV and no photon with $p_T > 1.5$ GeV.

The isolation cone has a ΔR of 0.5, and the signal cone of 0.15 for photons and $5.0/E_T$ for charged hadrons in which the E_T is of the pf-tau jet. As an addition the ΔR must be between 0.07 and 0.15. More information about the tau reconstruction can be found in reference [12].

The used background, signal and data sets for the study of the hadronic jets are the same used for the W' decaying to tau and further to electron and are listed there in section 7.1.1, because many jets include electrons and are therefore in this data set.

The used samples for the particle-flow taus are from the official 'Summer 2011' production, because the number of generated events is different from the 'Spring 2011' Monte Carlo samples used for the previous three channels, the used samples and their properties are listed below in table 8.1. All the available samples for the electron channel were used.

background	generator (p_T binning [GeV])	cross-section [pb]	number of events
$W \to e\nu$	PYTHIA ($p_T < 100$)	10438	5334220
$W \to e\nu$ (high p_T)	PYTHIA ($p_T > 100$)	1.569	1074060
$W \to \tau\nu$	PYTHIA	10438	5500000
$W \to \mu\nu$	PYTHIA	10438	5413258
$t\bar{t}$	Madgraph	157.5	1164208
QCD	PYTHIA ($20 < p_T < 30$)	2454400	3000000
	PYTHIA ($30 < p_T < 80$)	3671200	3000000
	PYTHIA ($80 < p_T < 170$)	139500	8130672
Drell-Yan	PYTHIA ($Z \to ee$)	1666	2262653
	PYTHIA ($Z \to \mu\mu$)	1666	2148325
	PYTHIA ($Z \to \tau\tau$)	1666	2032536

Table 8.1: Background samples for hadronic jets and particle-flow taus

The signal samples used for the hadronic jets and particle-flow taus have changed as well and are listed in table 8.2.

W' mass [GeV]	cross-section [pb]	number of events
1500	0.0949	16500
2000	0.0135	16500
2200	0.0066	16500
2500	0.0025	16500

Table 8.2: Signal samples

The used data set is the same used for electrons and are listed in table 7.4.

The M_T-distributions for both channels are shown in figures 8.1 and 8.2.

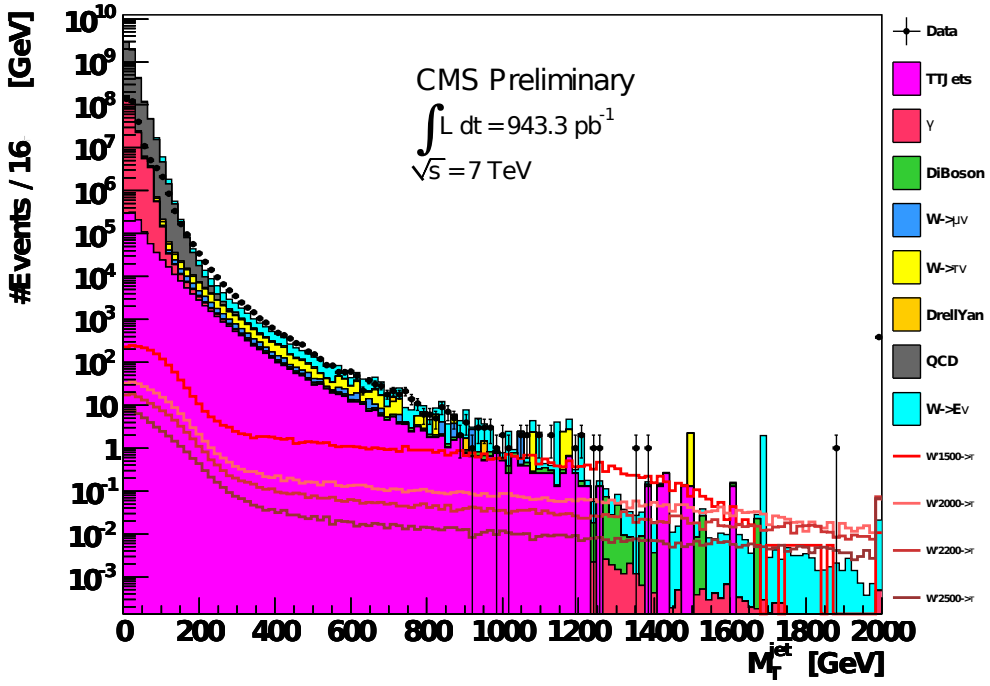

Figure 8.1: Jet raw data: The difference between data and background Monte Carlo samples can be explained by the different triggers used for the skimming of the data and background samples.

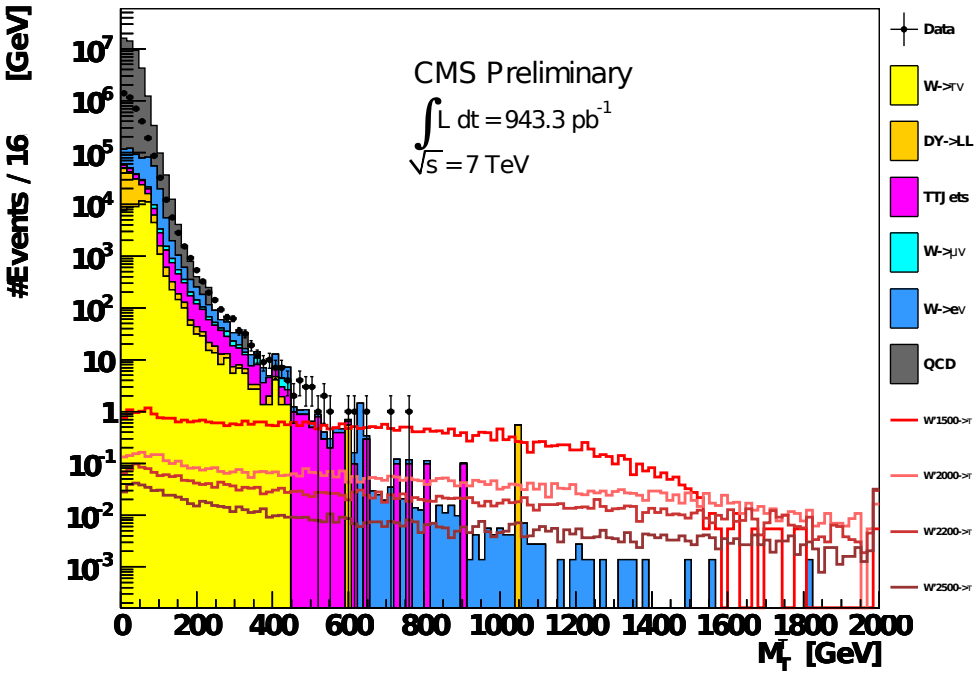

Figure 8.2: Particle-flow tau raw data: The same difference between data and Monte Carlo samples as for the jets can be seen, and is expected, because the particle-flow taus are reconstructed out of jets.

To isolate the jets and particle-flow taus from high energy taus some quality cuts are necessary. The used cuts are explained in the following section.

8.3 QUALITY CUTS

The used quality cuts for the hadronic jets are briefly explained in the following and the cutflow can be seen in figure 8.3.

1. fired electron trigger
   the used triggers are listed in table A.4 (an electron trigger is used because the samples are skimmed to contain electrons).

2. Jet_ID
   jet quality criteria explained below.

3. $E_T^{jet} > 30GeV$ cut, because of the trigger

4. $|\eta| < 3.0$ cut

5. some kinematic cuts explained in detail in the next section.

6. single Jet cut

The Jet ID is already implemented in the skimmer and checks if a jet fulfills the jet quality cuts 'pureo9' in the region 'lose' [2]. The used cuts are short explained below.

- for all jets: $\begin{cases} f_{HPD} < 0.98 \\ N^{90}_{hits} \geqslant 2 \end{cases}$
- for jets with $|\eta| < 2.55$: $f_{EM} > 0.01$
- for jets with $|\eta| > 2.55$: $f_{EM} > -0.9$
- for jets with $|\eta| > 2.55$ and $p_T > 80$ GeV: $-0.9 < f_{EM} < 1$

In there N^{90}_{hits} is the minimal number of reconstructed hits containing 90% of the jet energy, f_{HPD} the fraction of energy in the most energetic hybrid photo-diode(HPD) readout and f_{EM} is the fraction of energy measured in the Ecal. A more detailed description of these cuts and how they work can be found in [20]. How this and the other cuts work on the different background samples can be seen in the following cutflow.

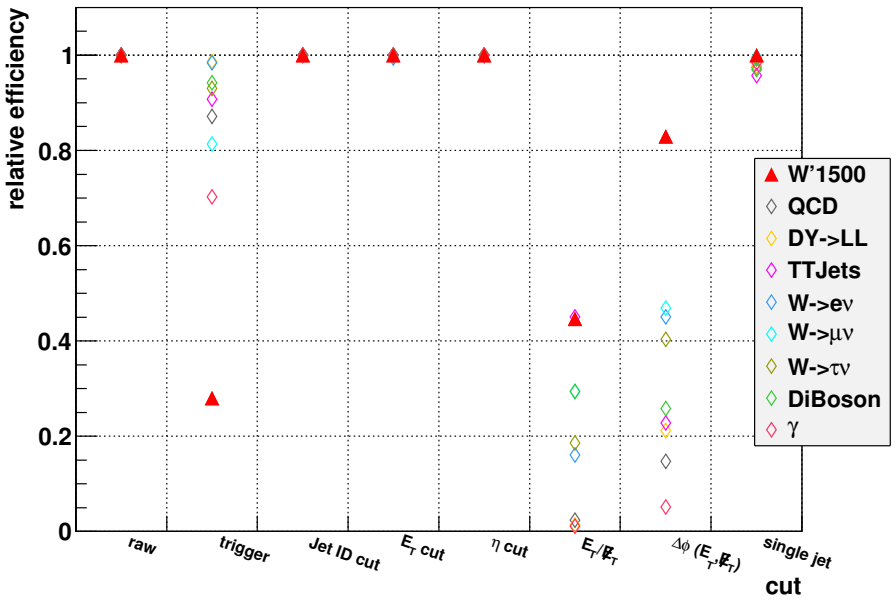

Figure 8.3: Jet cutflow

In this cutflow we can see that we loose much signal in the trigger cut, that is because the background samples are skimmed so that in each event an electron trigger should have fired. The signal sample contains all events so we loose much because of the trigger cut. We have also checked the alternative to the electron trigger, a single Jet trigger, but it worked very different on background Monte Carlo and data events and was therefore

not used. It is obvious that this cut has very much potential for optimization.

The particle flow taus are an alternative approach to get the hadronic decaying taus but the taus can not be fully reconstructed because of the undetected neutrinos, so we use some simple cuts to get a good signal to background ratio. The used cuts are short explained in the following and the corresponding cutflow can be seen in figure 8.4.

1. fired tau trigger and at least one electron
   the used triggers are listed in table A.4 in the appendix.
2. $|\eta| < 3.0$
   necessary because of the geometric acceptance of CMS.
3. $d_{vtx1} < 0.001$
   d_{vtx1}: distance between the point of the tau origin and the interaction point
4. $d_{vtx2} > 0.4$
   d_{vtx2}: distance between the point of the tau decay and the interaction point
5. single tau cut
6. $0.8 < E_T/\not{E}_T < 1.2$
7. $\Delta\varphi > 2.8$

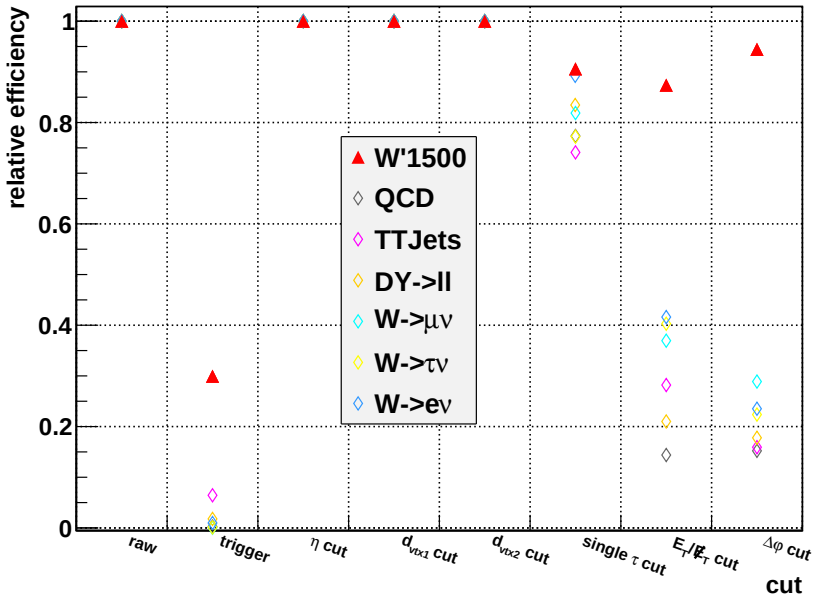

Figure 8.4: Particle-flow tau cutflow

Because all background and signal samples have been skimmed to contain an electron, we require at least one electron in the first

cut so that the signal is comparable to the background. Because of that we loose very much signal in the trigger cut.

To get a better signal to background ratio we next want to implement some quality cuts.

8.4 KINEMATICS

From the generator level study (see section 6.1) we know, that as in the leptonic channels the expected value of $\Delta\varphi$ and $E_T/\not{E}_T$ but not the best cut values to cut around them. To get these cut values we made the same calculation as in the leptonic channels, which means varying the cut values and calculating the signal over background ratio. As an example the upper $E_T/\not{E}_T$ cut value is shown in figure 8.5. For this study the lower cut value was set to zero and the upper one was varied from 0.1 up to 2.0 in 0.1 steps. The calculated efficiency for each cut value and the signal over background and signal over square-root of background ratios are calculated. The plots for the other two cut values can be found in the appendix (A.9 and A.11).

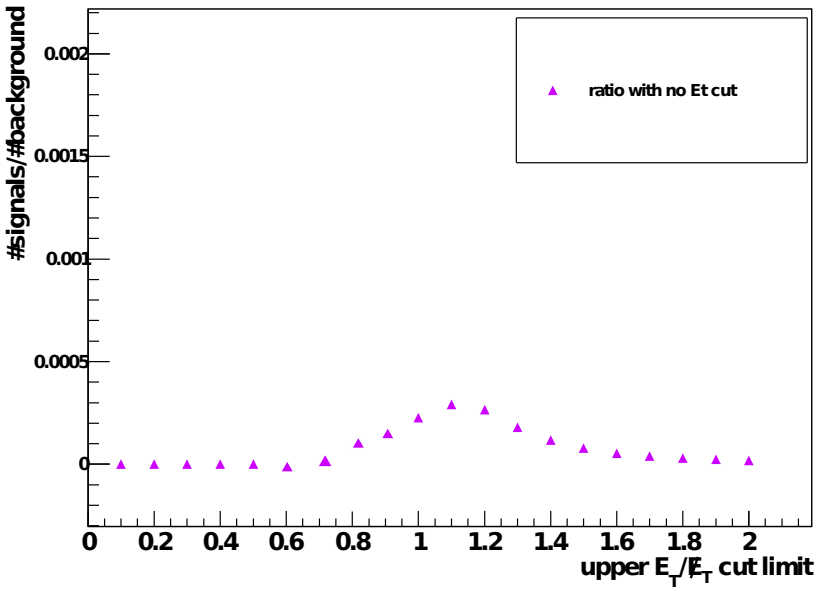

Figure 8.5: Upper $E_T/\not{E}_T$ cut jets: We can see a shift of the bump to an $E_T/\not{E}_T$ ratio slightly higher than 1, because of lower missing transverse energy in this events.

From this signal to background ratio and the plots for the other two cut cut value we get the following cut values:

1. $\Delta\varphi > 2.8$
2. $0.8 < E_T/\not{E}_T < 1.2$

The cut values can be used for both hadronic channels, because the particle-flow taus are a subset of the hadronic jets.

8.5 RESULTS

With all these cuts we get the distribution shown in figure 8.6 for the hadronic jets and the distribution in figure 8.7 for the particle-flow taus the different stages after each cut can be seen in the appendix (see section A.7 for the hadronic jets and section A.8 for the particle-flow taus).

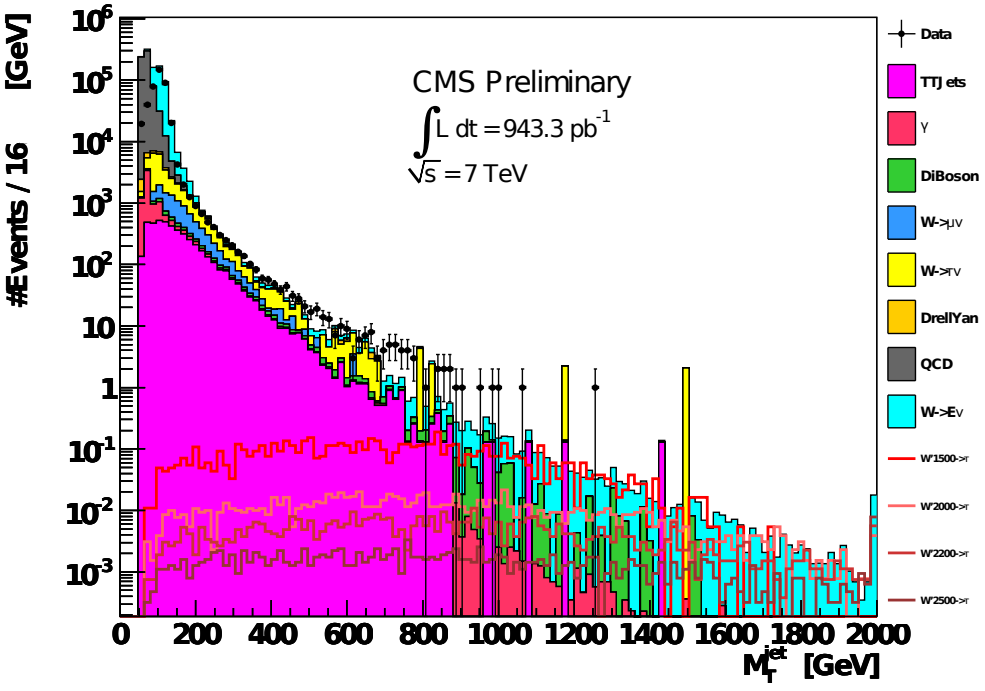

Figure 8.6: Resulting jet data: As in the leptonic decays of the tau, we can clearly see the Standard Model W peak, but no characteristic peak in the signal distribution.

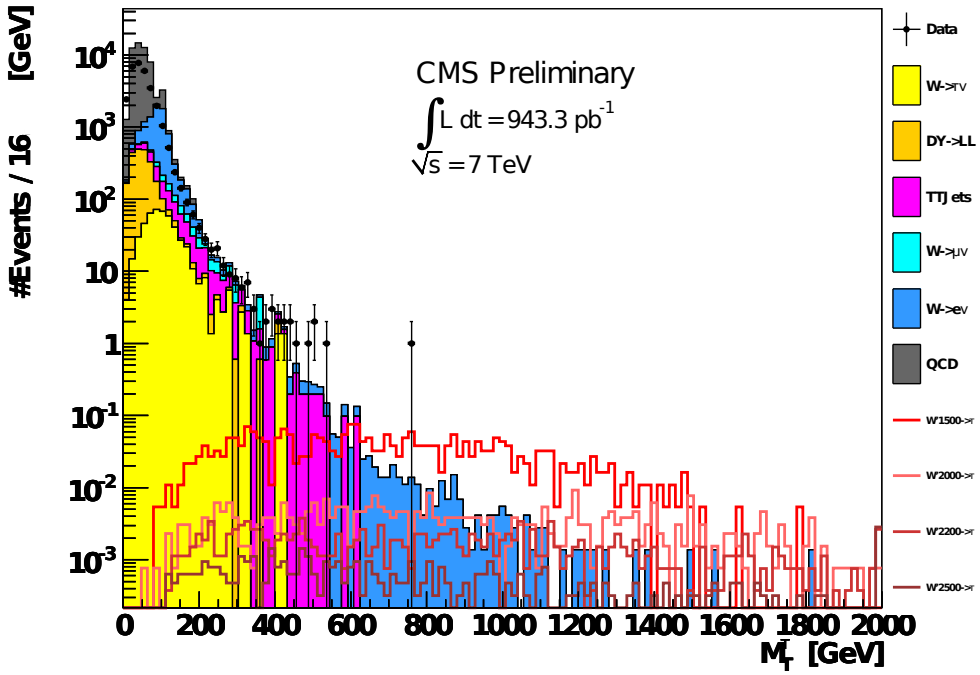

Figure 8.7: Resulting particle-flow tau data: The distribution looks very similar to the one for the hadronic jets, with two major differences, first that we have only 1/10 of the data because many events contain jets but much less are tau-like. Second because the signal is quite similar to the hadronic jets a much higher signal to background ratio in the high M_T region.

In both distributions we can see no signal of a W', so we can only calculate an exclusion limit. But because we are using the electron data and background samples this limit is directly correlated with the leptonic channels, but the difference between hadronic jets and particle-flow taus will show the possible advantage of one channel.

As in the leptonic channels we calculate a limit on the cross-section by making a last cut on M_T of $M_T > 250$ GeV for the hadronic jets and $M_T > 350$ GeV for the particle-flow taus. The final limit plots for the hadronic jets and particle-flow taus are shown in figure 8.8.

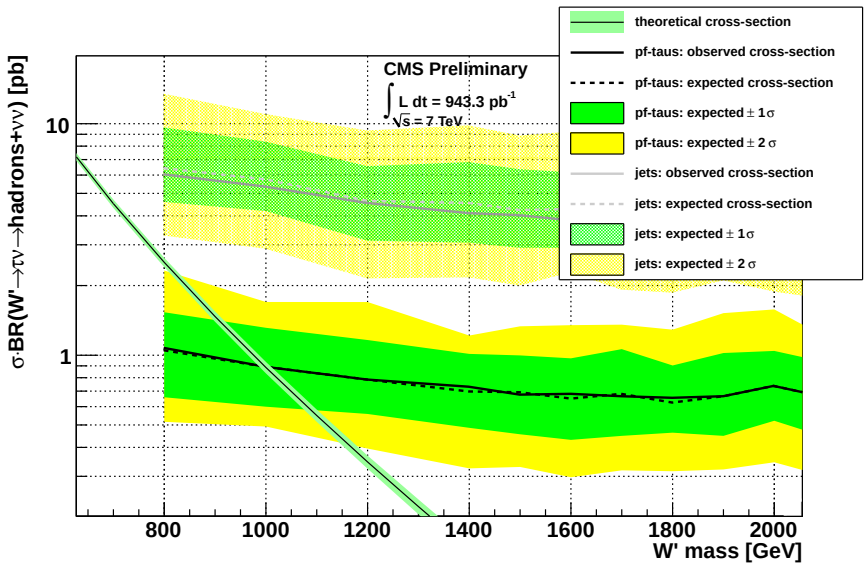

Figure 8.8: Hadronic limit plot: We can see that the observed limit for the hadronic jets has no intersection with the theoretical cross-section, and can only guess that it is around 600 GeV, because we had no samples with a so low W′ mass. Contrary to that we can get a clear mass limit of $m_{W'} > 1000$ GeV for the particle-flow taus.

From this limit plot we can clearly conclude that the particle-flow taus are a much better way to study the hadronic decaying taus. To have a further look into the possibilities of the particle-flow taus in then next section we had a look at a few different quantities of the particle-flow taus.

8.6 PARTICLE-FLOW TAUS

The first quantity which is also important for the other channels is the flight distance of the tau, that is the distance the tau flies before it decays. All quantities were checked with a W′ sample with a mass of 1500 GeV. For the particle flow taus the vertex were the tau decays is reconstructed as the reconstructed vertex of the leading charged hadron and should be the tau vertex, so we can calculate the distance to the interaction point and get the flight distance. To get an expectation we first calculate the flight distance theoretically. The flight distance d is because of the time dilation the mean life time T_0 times the speed of light c_0 (because of the strong boost from the tau) times the relativistic gamma factor:

$$d = T_0 \cdot c_0 \cdot \gamma \tag{8.1}$$

Gamma being in natural units defined as:

$$\gamma = \frac{E}{M_0} \tag{8.2}$$

With the values of the tau ($T_0 = 291 \cdot 10^{-15}$ s, $M_0 = 1.777$ GeV, see ref. [16]) and the mean energy $E = 750$ GeV for a tau coming from a W' with a mass of 1500 GeV, we get a flight distance d of:

$$d = 3.7 \text{ cm}. \tag{8.3}$$

This value is only an estimation because the decay is a statistical process and only the mean energy is 750 GeV, so not every particle has the energy or lives $291 \cdot 10^{-15}$ s. The measured distribution of the distance of reconstructed vertex (the point where the tau decays) to the interaction point is shown in figure 8.9 and fits our expectation. Compared to the first layer of the pixel detecter, which is in a distance of 4.4 cm to the beam pipe, not many taus will reach it and can be detected there, because if they get a boost in the z-direction the probability to reach the pixel detector is even smaller.

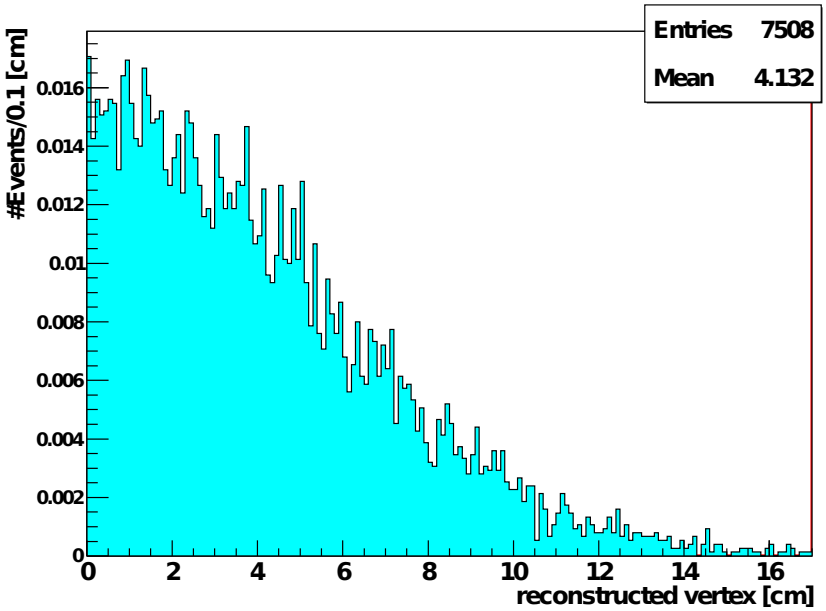

Figure 8.9: Measured distance the tau flew from the interaction point to its decay point.

The second quantity we want to have a look at is the hadronic decay mode of the tau.

The particle-flow tau algorithm reconstructs the tau out of its hadronic decay products so we also know the decay mode of

the tau, and we want to check how these measurement matches the theoretical values. The measured decay modes are shown in figure 8.10.

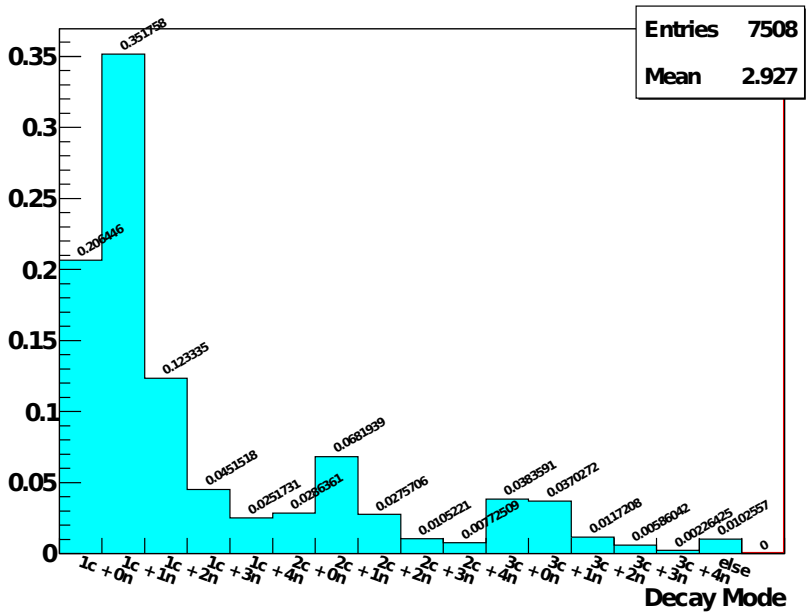

Figure 8.10: Measured hadronic decay modes of the tau (explanation for the x-axis: the number of charged and neutral particles are listed e.g 3c + 2n means there were three charged and two neutral particles reconstructed).

To compare the measured values to the theoretical ones they are all listed in table 8.3. The measured values shown in figure 8.10 are relative to all hadronic decays, the theoretical values are relative to all decay modes. Because of that the measured values are shown with respect to all decays as well.

decay mode	measured ratio [%]	theoretical ratio [%] (see ref. [16])
1 charged + 0 neutral	13.5	11.61 ± 0.06
1 charged + 1 neutral	23.0	25.94 ± 0.09
1 charged + 2 neutral	8.1	9.51 ± 0.11
1 charged + 3 neutral	2.9	1.18 ± 0.08
1 charged + 4 neutral	1.6	$(2.6 \pm 0.4) \cdot 10^{-3}$
2 charged + 0 neutral	1.9	N/A
2 charged + 1 neutral	4.5	
2 charged + 2 neutral	1.8	
2 charged + 3 neutral	0.7	
2 charged + 4 neutral	0.5	

decay mode	measured ratio [%]	theoretical ratio [%] (see ref. [16])
3 charged + 0 neutral	2.5	9.8 ± 0.08
3 charged + 1 neutral	2.4	4.75 ± 0.06
3 charged + 2 neutral	0.8	$(5.06 \pm 0.32) \cdot 10^{-3}$
3 charged + 3 neutral	0.4	$(2.3 \pm 0.7) \cdot 10^{-4}$
3 charged + 4 neutral	0.1	N/A
else	0.7	

Table 8.3: Comparison between measured and theoretical hadronic decay modes relative to all decay modes.

In this comparison we can see that the reconstruction does not reconstruct all particles, because of that there are also two charged particles measured, which is not possible because of the conversation of charge and the charged tau lepton.

The last quantity we want to have a look at is how efficient the particle-flow algorithm selects the taus, for that we simply compare the number of reconstructed taus with the number of generated events. The calculated efficiency can then be compared to the theoretical branching ratio for the tau decaying hadronically. The results are shown in table 8.4.

generated events	16500
reconstructed particle-flow taus	7169
efficiency [%]	43.4
theoretical branching ratio [%]	65.29 ± 0.05
ratio: measured to theoretical value [%]	66.5

Table 8.4: Particle-flow tau efficiency

With this simple method we can see that about 67% of the hadronic decaying taus are reconstructed as particle-flow taus. The algorithm tries to exclude "normal" jets to be reconstructed as particle-flow taus and therefore excludes also some tau-jets. A possibility for a better reconstruction of the taus is to try different reconstruction algorithms supplementary to the shrinking cone algorithm used here.

9

CONCLUSION

As a conclusion we can say that the well understood leptonic channels are not the best way to search for a W′ decaying into a tau, because the distinction between leptons coming from the tau decay and the leptons coming directly from a W′ decay is not easy. If we can not distinguish between them at all, we can see the leptonic channels as an additional signal to the $W' \to e\nu$ and $W' \to \mu\nu$ channels, which could be seen as a higher than expected signal in the lower M_T-region.

If we assume that we can distinguish between the leptons we see no signal that indicates a W′ and therefore calculate a mass exclusion limit. For that we can either assume the equal branching ratios in the three leptonic decay modes of the Reference Model (see ref. [17]) and get a mass limit of $m_{W'} > 1150$ GeV or we assume that the W′ decays leptonic only in tau and get a mass limit of $m_{W'} > 1500$ GeV.

At last we had an additional look at the hadronic decaying taus, by looking at the hadronic jets and the particle-flow taus. We can conclude that the particle-flow taus are a much better way to study the hadronic decaying taus, and that the reconstruction algorithm also reconstructs flight distance and decay mode of the tau.

Especially in the hadronic decay modes are much possibilities for further studies, by having a look at different tau reconstruction algorithms and a optimization of the used cuts. But already this first look at the hadronic decaying taus indicates that they can be a valuable addition to the at the moment studied leptonic channels.

Part I

APPENDIX

A

APPENDIX

A.1 GENERATOR LEVEL

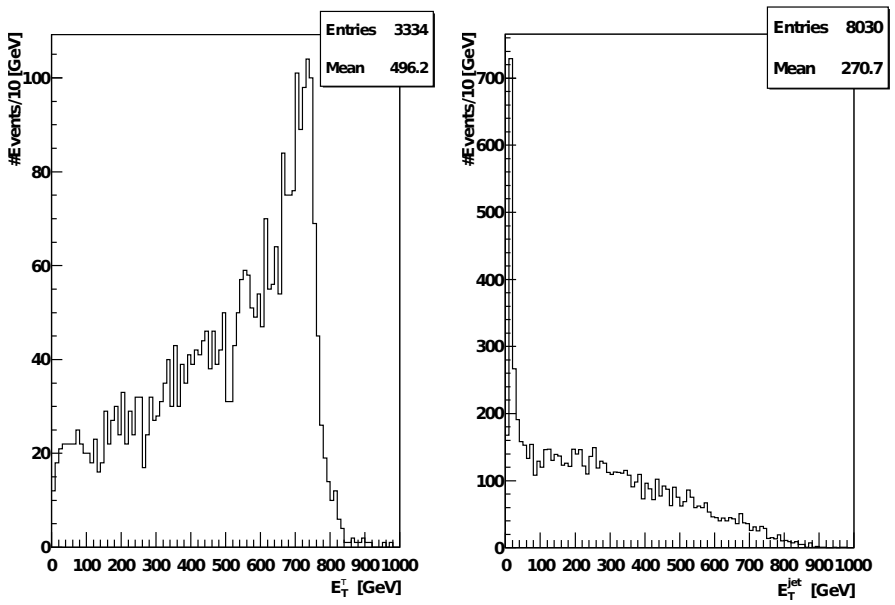

Figure A.1: E_T^τ vs. E_T^{jet}: Transverse energy distribution for the tau coming from the W′ and the jet coming from the tau.

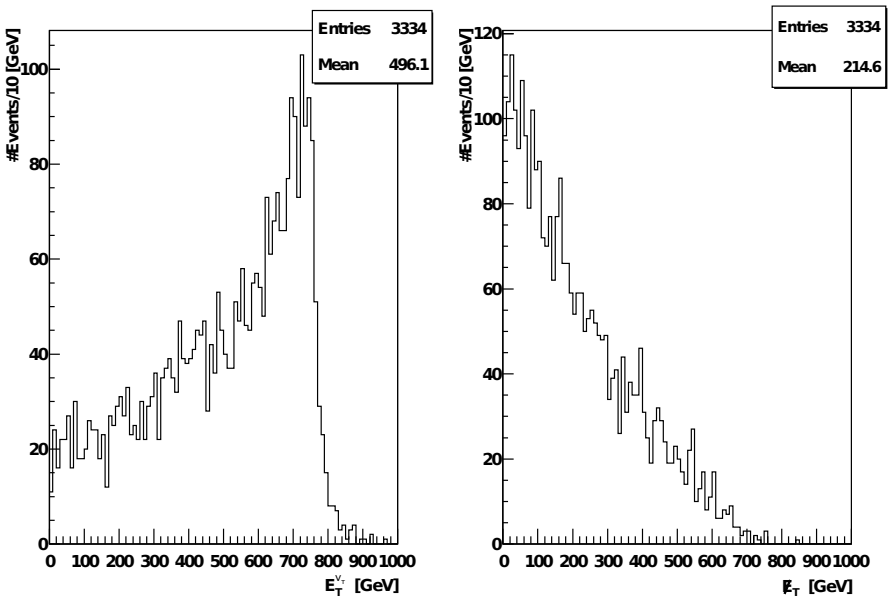

Figure A.2: $E_T^{\nu_\tau}$ vs. $\not{E}_T$: Transverse energy of the neutrino coming from the W′ decay and the missing transverse energy calculated out of the three neutrinos in a leptonic decaying tau.

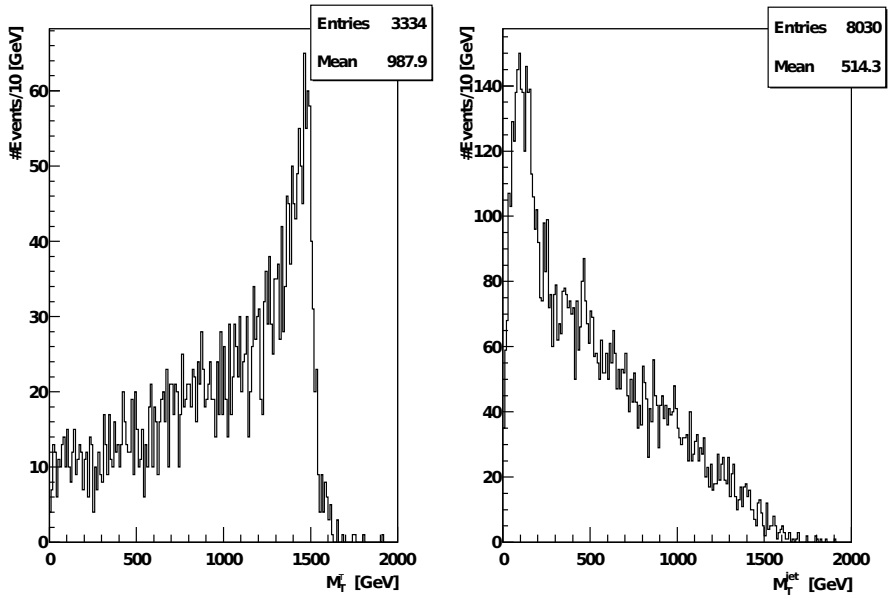

Figure A.3: M_T^τ vs. M_T^{jets}: Transverse mass of the tau and neutrino from the W′ decay and transverse mass calculated out of the hadronic jet coming from the tau decay and the two neutrinos in the event as missing transverse energy.

The different distributions for the kinematic cuts.

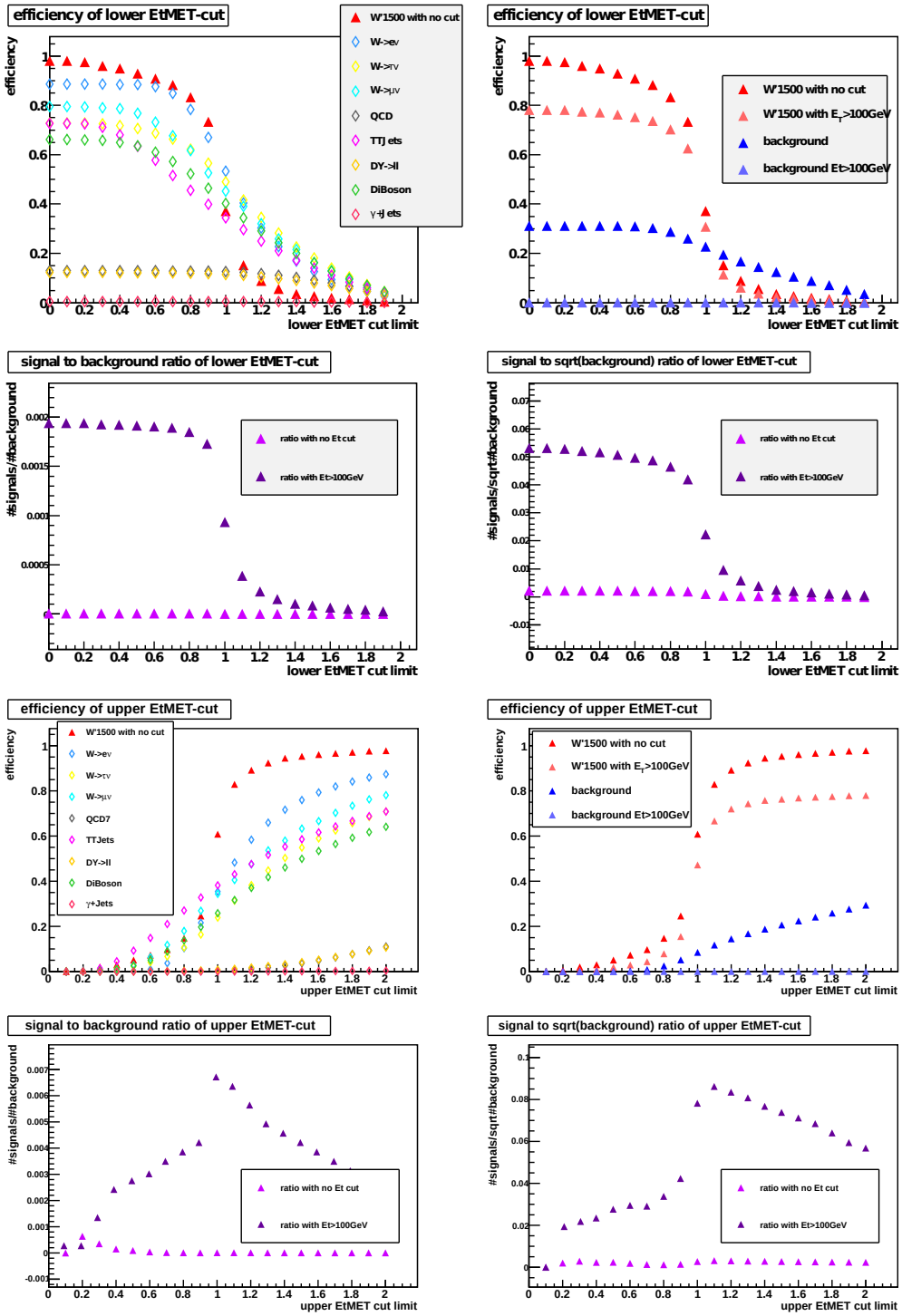

Figure A.4: Electron $E_T/\not{E}_T$ cut

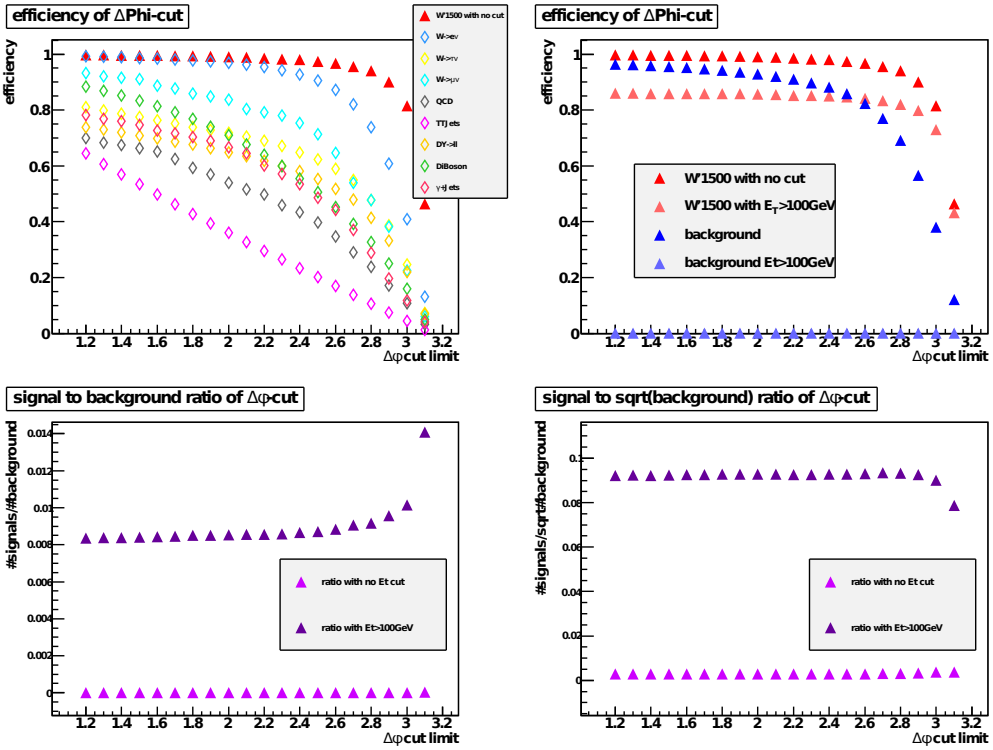

Figure A.5: Electron $\Delta\varphi$ cut

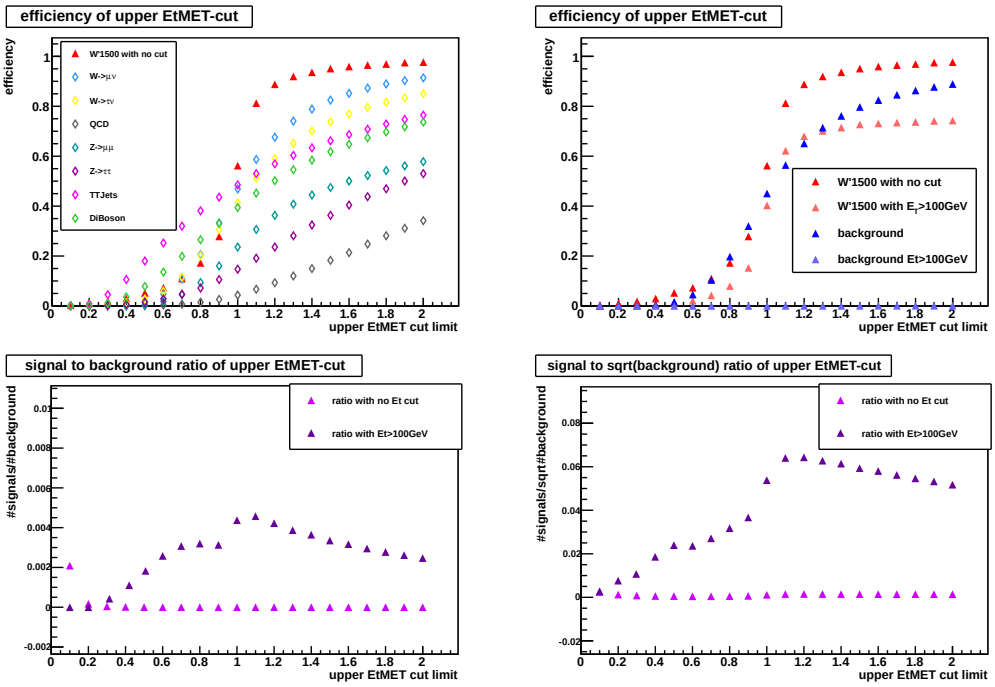

Figure A.6: Muon upper $E_T/\not{E}_T$ cut

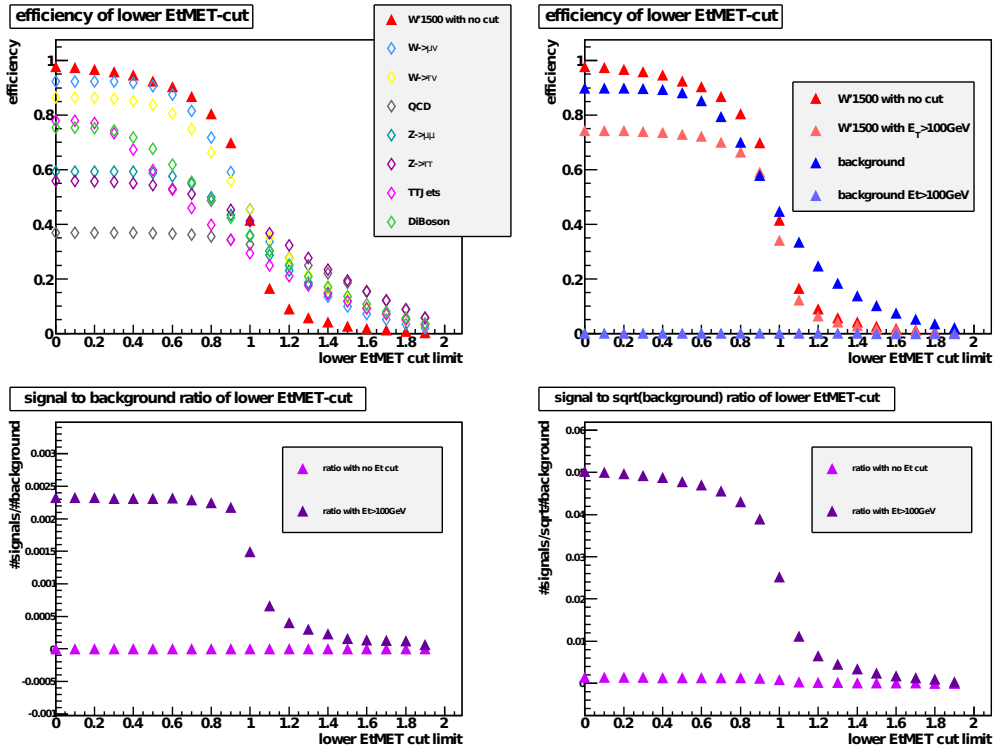

Figure A.7: Muon lower $E_T/\not{E}_T$ cut

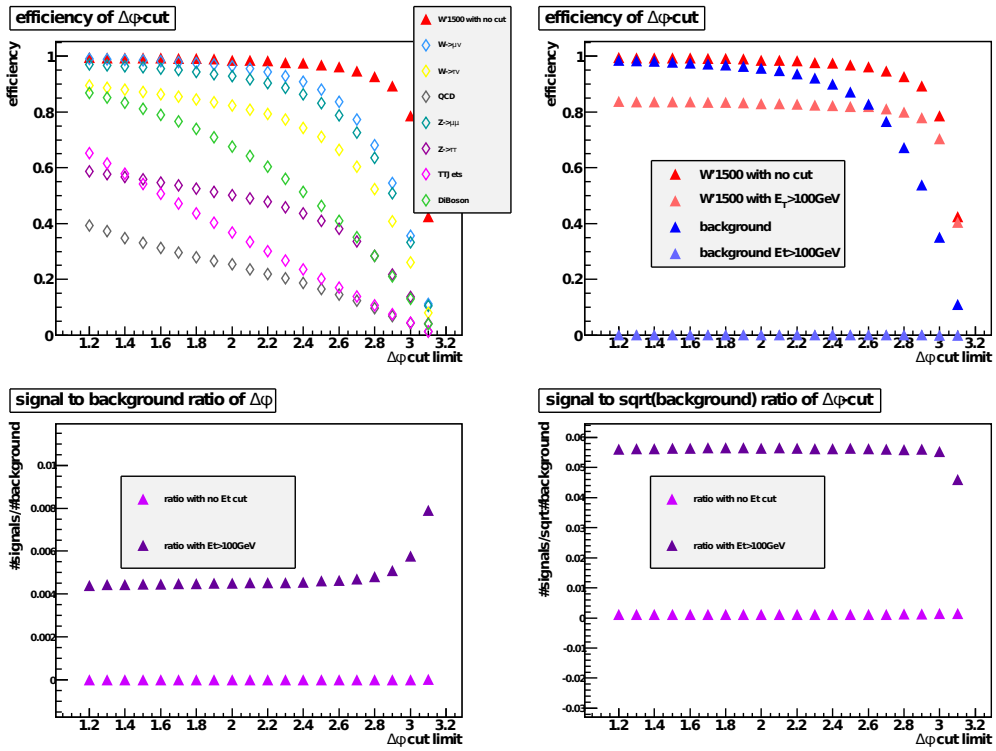

Figure A.8: Muon $\Delta\varphi$ cut

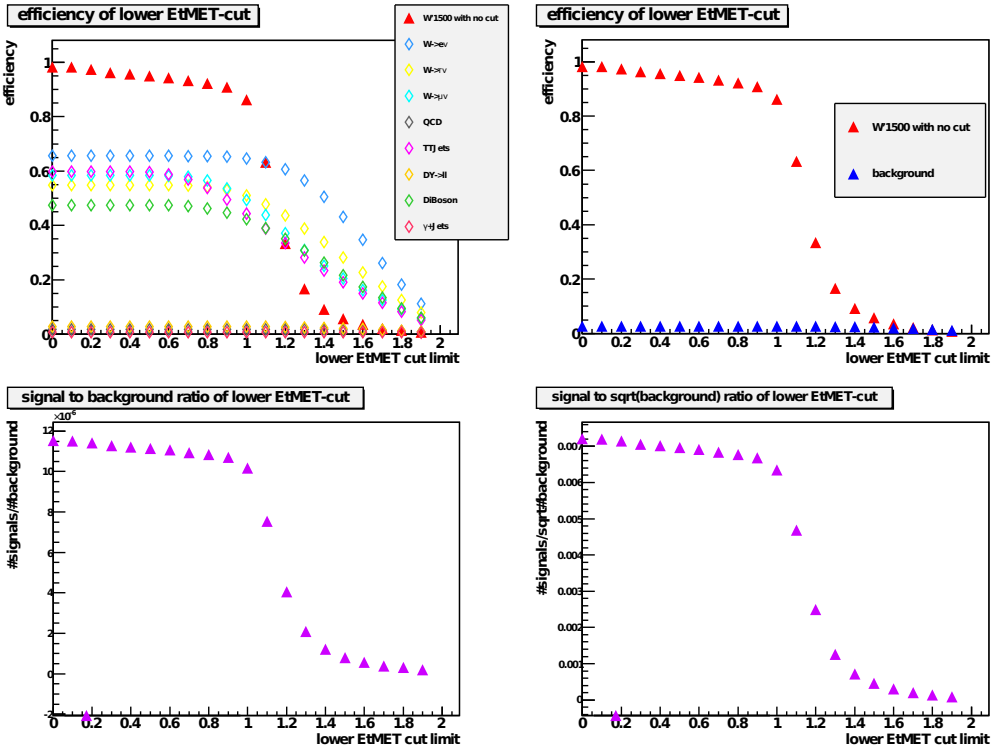

Figure A.9: Jet lower $E_T/\not{E}_T$ cut

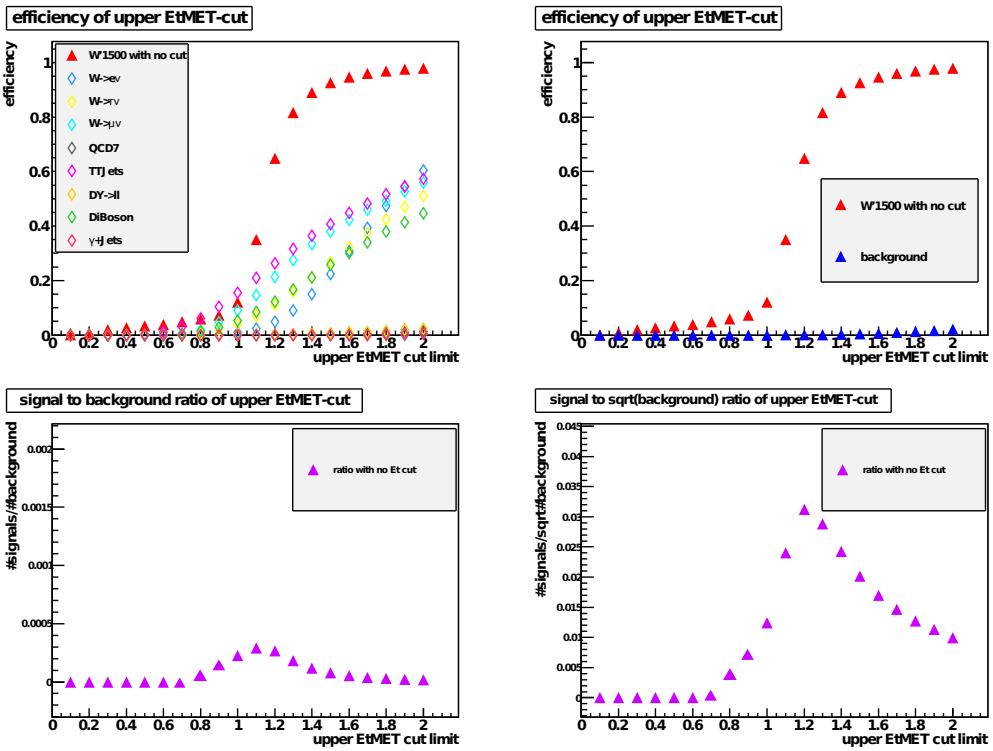

Figure A.10: Jet upper $E_T/\not{E}_T$ cut

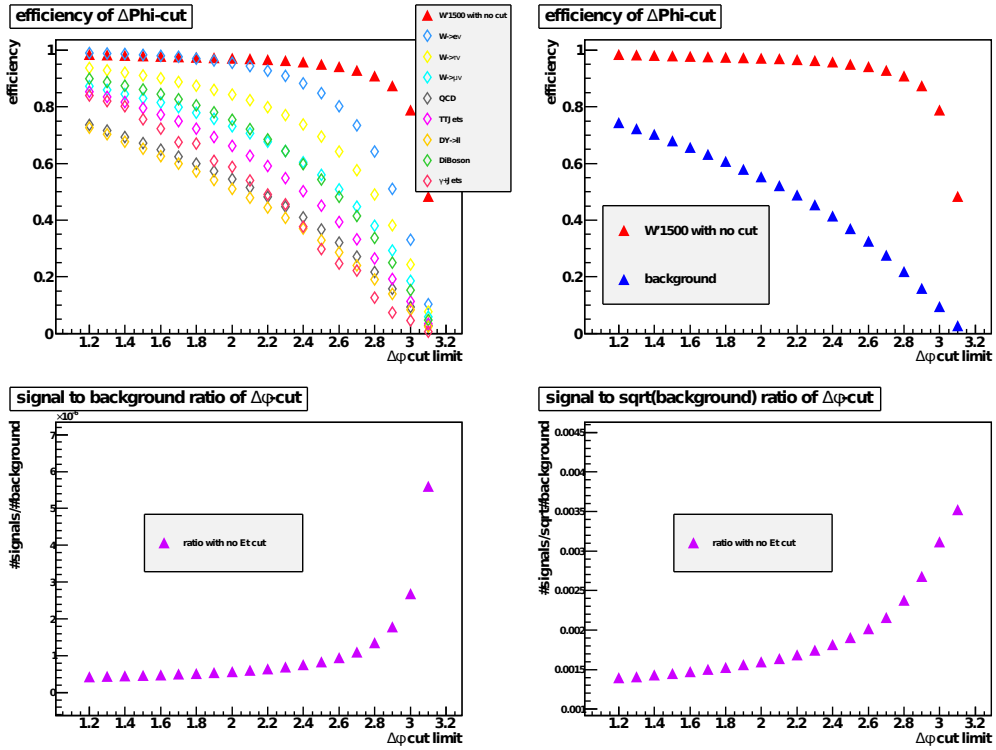

Figure A.11: Jet $\Delta\varphi$ cut

Process (p_T binning [GeV])	Dataset name
$W \rightarrow e\nu$	/WToENu TuneZ2 7TeV-pythia6/Summer11-PU S3 START42 V11-v2/AODSIM
$W \rightarrow e\nu$ $(p_T > 100)$	/WToENu ptmin-100 TuneZ2 7TeV-pythia6/Summer11-PU S4 START42 V11-v1/AODSIM
$W \rightarrow \mu\nu$	/WToMuNu TuneZ2 7TeV-pythia6/Summer11-PU S3 START42 V11-v2/AODSIM
$W \rightarrow \tau\nu$	/WToTauNu TuneZ2 7TeV-pythia6-tauola/Summer11-PU S3 START42 V11-v2/AODSIM
$t\bar{t}$	/TTJets TuneZ2 7TeV-madgraph-tauola/Spring11-PU S1 START311 V1G1-v1/AODSIM
QCD $(20 < p_T < 30)$	QCD Pt-20to30 EMEnriched TuneZ2 7TeV-pythia6/Spring11-PU S1 START311 V1G1-v1/AODSIM
QCD $(30 < p_T < 80)$	QCD Pt-30to80 EMEnriched TuneZ2 7TeV-pythia6/Spring11-PU S1 START311 V1G1-v1/AODSIM
QCD $(80 < p_T < 170)$	QCD Pt-80to170 EMEnriched TuneZ2 7TeV-pythia6/Spring11-PU S1 START311 V1G1-v1/AODSIM
WZ	/WZtoAnything TuneZ2 7TeV-pythia6-tauola/Spring11-PU S1 START311 V1G1-v1/AODSIM
ZZ	/ZZtoAnything TuneZ2 7TeV-pythia6-tauola/Spring11-PU S1 START311 V1G1-v1/AODSIM
WW	/WWtoAnything TuneZ2 7TeV-pythia6-tauola/Spring11-PU S1 START311 V1G1-v1/AODSIM
$\text{Drell} - \text{Yan}(Z \rightarrow ee)$	/DYToEE M-20 TuneZ2 7TeV-pythia6/Summer11-PU S3 START42 V11-v2/AODSIM
Drell-Yan $(Z \rightarrow \mu\mu)$	/DYToMuMu M-20 TuneZ2 7TeV-pythia6/Summer11-PU S3 START42 V11-v2/AODSIM
Drell-Yan $(Z \rightarrow \tau\tau)$	/DYToTauTau M-20 TuneZ2 7TeV-pythia6-tauola/Summer11-PU S3 START42 V11-v2/AODSIM
$\gamma + \text{Jets}$ $(0 < p_T < 15)$	/G Pt 0to15 TuneZ2 7TeV pythia6/Spring11-PU S1 START311 V1G1-v1/AODSIM
$\gamma + \text{Jets}$ $(15 < p_T < 30)$	/G Pt 15to30 TuneZ2 7TeV pythia6/Spring11-PU S1 START311 V1G1-v1/AODSIM
$\gamma + \text{Jets}$ $(30 < p_T < 50)$	/G Pt 30to50 TuneZ2 7TeV pythia6/Spring11-PU S1 START311 V1G1-v1/AODSIM
$\gamma + \text{Jets}$ $(50 < p_T < 80)$	/G Pt 50to80 TuneZ2 7TeV pythia6/Spring11-PU S1 START311 V1G1-v1/AODSIM
$\gamma + \text{Jets}$ $(80 < p_T < 120)$	/G Pt 80to120 TuneZ2 7TeV pythia6/Spring11-PU S1 START311 V1G1-v1/AODSIM
$\gamma + \text{Jets}$ $(120 < p_T < 170)$	/G Pt 120to170 TuneZ2 7TeV pythia6/Spring11-PU S1 START311 V1G1-v1/AODSIM
$\gamma + \text{Jets}$ $(170 < p_T < 300)$	/G Pt 170to300 TuneZ2 7TeV pythia6/Spring11-PU S1 START311 V1G1-v1/AODSIM
$\gamma + \text{Jets}$ $(300 < p_T < 470)$	/G Pt 300to470 TuneZ2 7TeV pythia6/Spring11-PU S1 START311 V1G1-v1/AODSIM
$\gamma + \text{Jets}$ $(470 < p_T < 800)$	/G Pt 470to800 TuneZ2 7TeV pythia6/Spring11-PU S1 START311 V1G1-v1/AODSIM
$\gamma + \text{Jets}$ $(800 < p_T < 1400)$	/G Pt 800to1400 TuneZ2 7TeV pythia6/Spring11-PU S1 START311 V1G1-v1/AODSIM
$\gamma + \text{Jets}$ $(1400 < p_T < 1800)$	/G Pt 1400to1800 TuneZ2 7TeV pythia6/Spring11-PU S1 START311 V1G1-v1/AODSIM
$\gamma + \text{Jets}$ $(1800 < p_T)$	/G Pt 1800 TuneZ2 7TeV pythia6/Spring11-PU S1 START311 V1G1-v1/AODSIM

Table A.1: Monte Carlo samples electron channel

Process (p_T binning [GeV])	Dataset name
$W^+ \to \mu^+\nu$	/WPlusToMuNu CT10 TuneZ2 7TeV-powheg-pythia/Spring11-PU S1 START311 V1G1-v1/AODSIM
$W^- \to \mu^-\nu$	/WMinusToMuNu CT10 TuneZ2 7TeV-powheg-pythia/Spring11-PU S1 START311 V1G1-v1/AODSIM
$W \to \mu\nu$ ($p_T > 100$)	/WToMuNu ptmin-100 7TeV-pythia6/Winter10-E7TeV ProbDist 2010Data BX156 START39 V8-v1/AODSIM
$W \to \tau\nu$	/WToTauNu TuneZ2 7TeV-pythia6-tauola/Summer11-PU S3 START42 V11-v2/AODSIM
WW	/ZZtoAnything TuneZ2 7TeV-pythia6-tauola/Spring11-PU S1 START311 V1G1-v1/AODSIM
WZ	/WZtoAnything TuneZ2 7TeV-pythia6-tauola/Spring11-PU S1 START311 V1G1-v1/AODSIM
ZZ	/WWtoAnything TuneZ2 7TeV-pythia6-tauola/Spring11-PU S1 START311 V1G1-v1/AODSIM
$t\bar{t}$	/TTJets TuneZ2 7TeV-madgraph-tauola/Spring11-PU S1 START311 V1G1-v1/AODSIM
QCD	/QCD Pt-20 MuEnrichedPt-15 TuneZ2 7TeV-pythia6/Spring11-PU S1 START311 V1G1-v1/AODSIM
Drell-Yan ($Z \to \mu\mu$)	/DYToMuMu M-20 TuneZ2 7TeV-pythia6/Summer11-PU S3 START42 V11-v2/AODSIM
Drell-Yan ($Z \to \tau\tau$)	/DYToTauTau M-20 TuneZ2 7TeV-pythia6-tauola/Summer11-PU S3 START42 V11-v2/AODSIM

Table A.2: Monte Carlo sample muon channel

Generator	W′ mass [GeV]	σ_{NNLO} [pb]	event numbers
PYTHIA	800	2.519	8700
PYTHIA	1000	0.886	16500
PYTHIA	1200	0.346	15960
PYTHIA	1400	0.144	15960
PYTHIA	1500	0.0949	16500
PYTHIA	1600	0.0633	16500
PYTHIA	1700	0.0423	16500
PYTHIA	1800	0.0285	16500
PYTHIA	1900	0.0193	16500
PYTHIA	2000	0.0135	16500
PYTHIA	2100	0.00937	12180
PYTHIA	2200	0.00661	16500
PYTHIA	2300	0.00472	16500
PYTHIA	2500	0.00248	14880
PYTHIA	2700	0.00143	16500
PYTHIA	3000	0.000707	16500
PYTHIA	3500	0.000296	13260
PYTHIA	4000	0.000146	16500

Table A.3: Signal samples

Trigger name	used for	channel
HLT_Ele22_SW_TighterEleId_L1R	'Spring 2011' MC	electron + hadronic
HLT_Mu21	'Spring2011' MC	muon
HLT_Ele90_NoSpikeFilter	data	electron + hadronic
HLT_Ele25_WP80	data	electron + hadronic
HLT_Ele32_CaloIdVT_CaloIsoT_TrkIdT_TrakIsoT	data	electron + hadronic
HLT_Mu24	data	muon
HLT_Mu30	data	muon
HLT_Ele27_CaloIdVT_CaloIsoT_TrkIdT_TrkIsoT	'Summer2011' MC	signal
HLT_Mu30	'Summer2011' MC	signal
HLT_IsoPFTau35_Trk20_MET45	'Summer2011'MC	pf-tau
HLT_IsoPFTau35_Trk20_MET45	data	pf-tau

Table A.4: All used triggers

Below the different electron M_T distributions for every cut are shown. The stage means the number of the cut as listed in the cut explanation (e.g Stage 1 is after cut 1: $E_T > 35$ GeV).

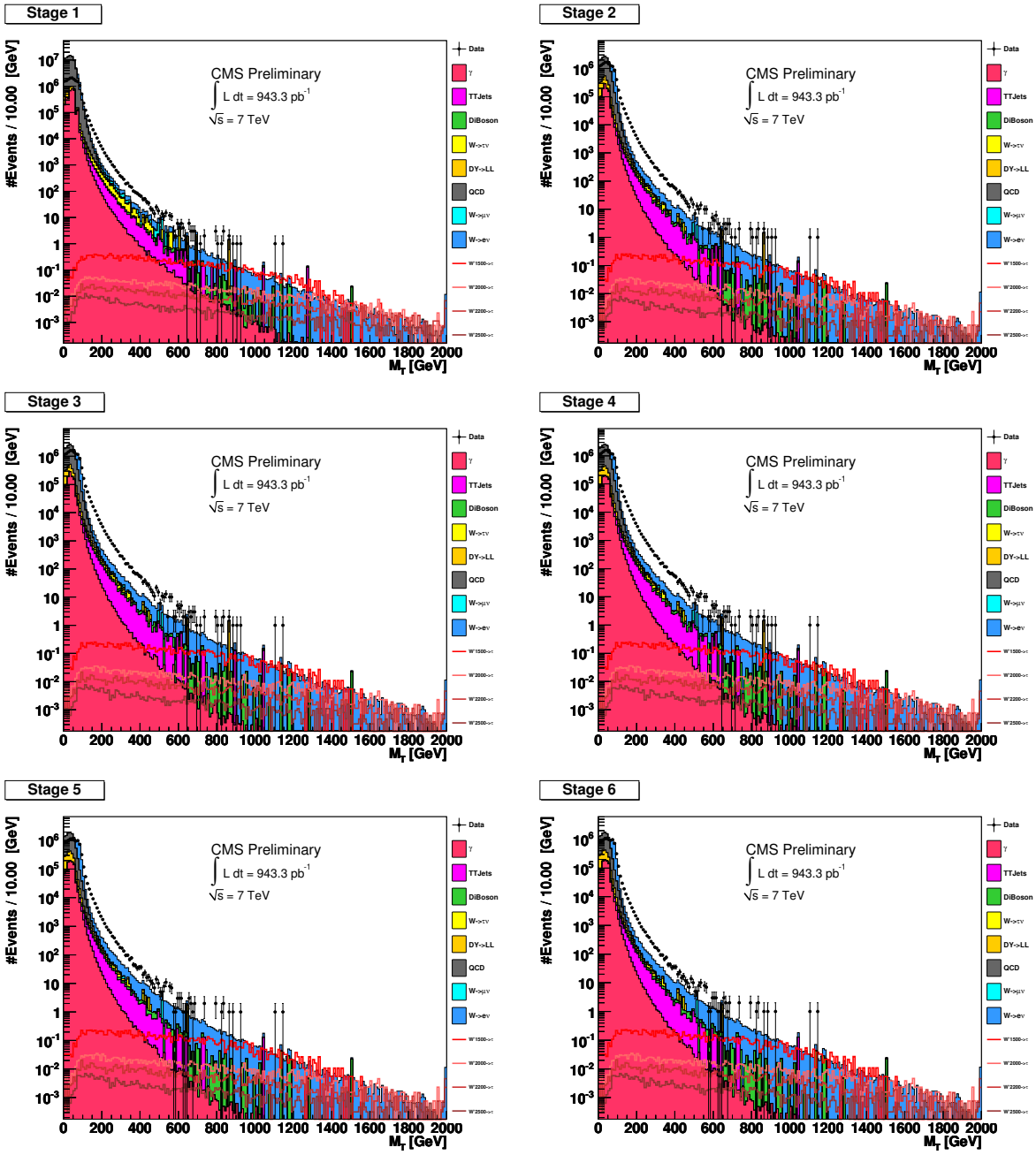

Figure A.12: Electron stages

Stage 7

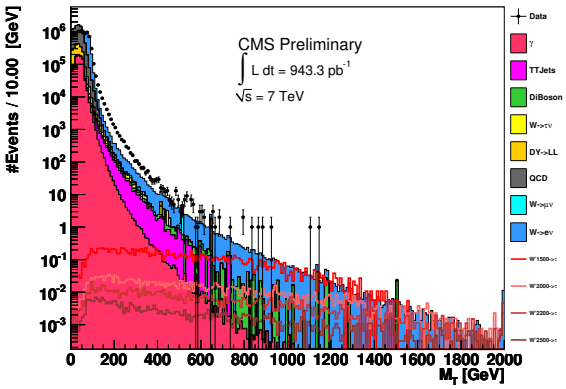

Stage 8

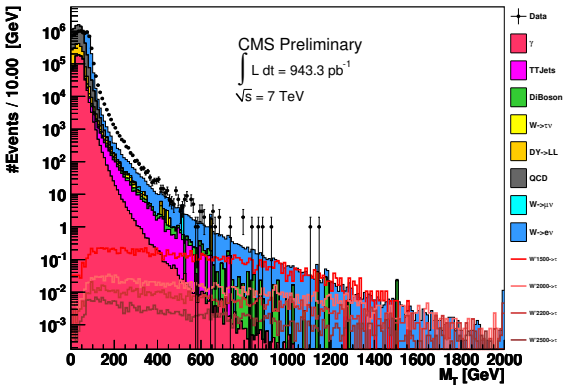

Stage 9

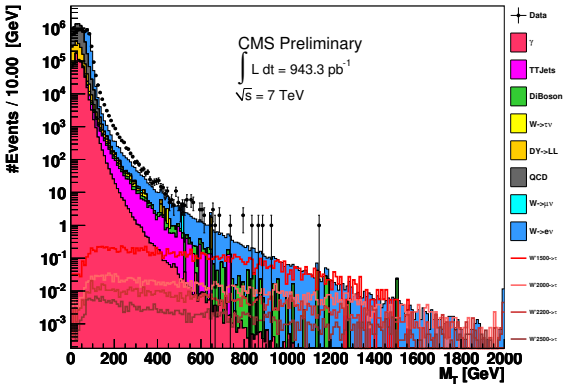

Stage 10

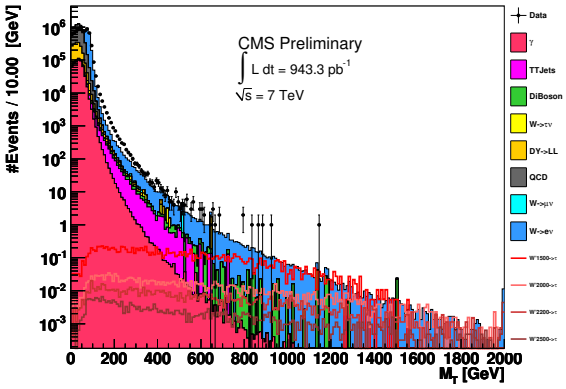

Stage 11

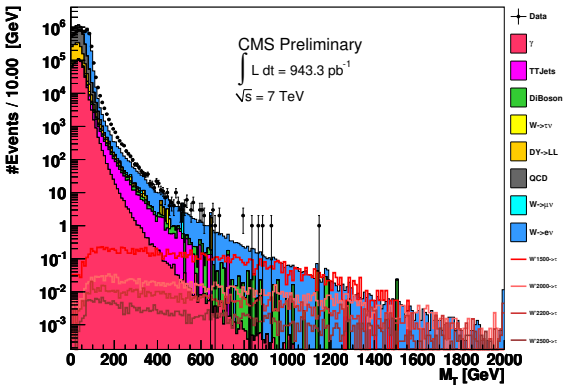

Stage 12

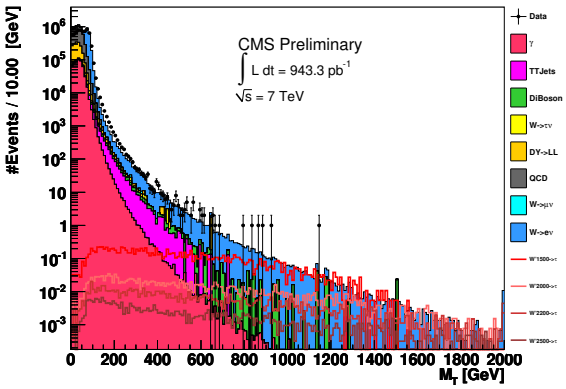

Stage 13

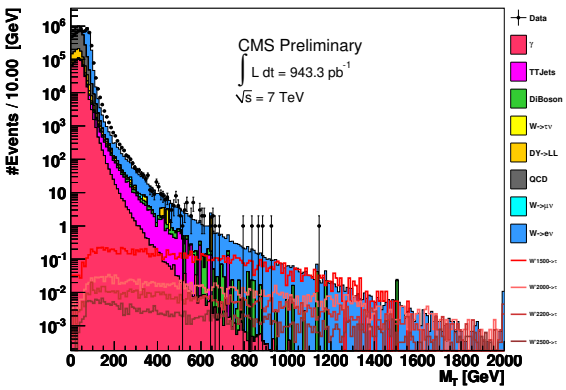

Stage 14

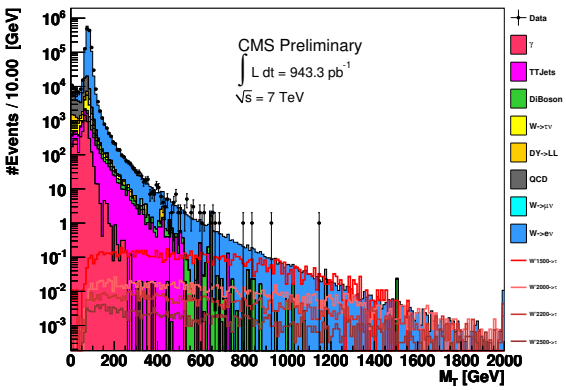

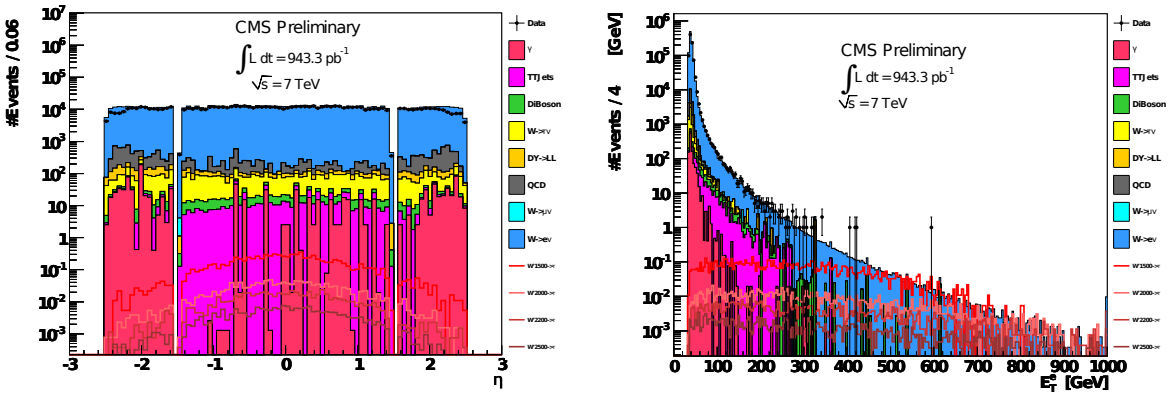

Figure A.13: Electrons: η and E_T distributions

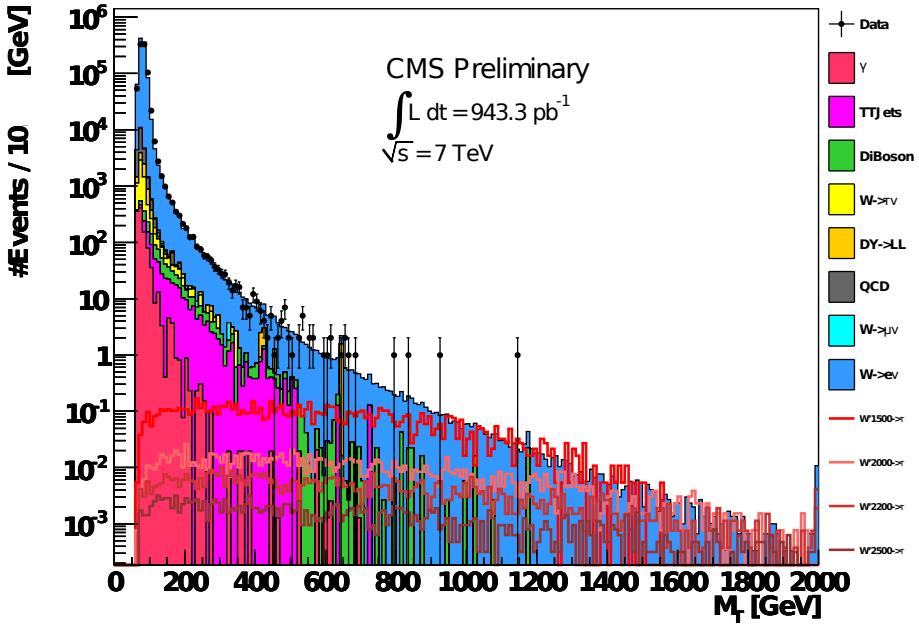

Figure A.14: Electron M_T-distribution after all quality and kinematic cuts

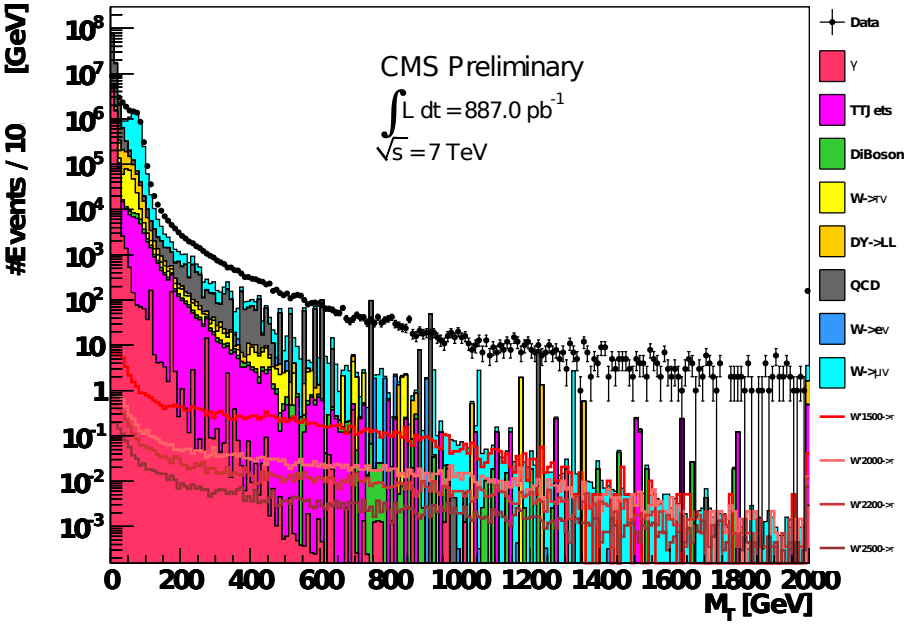

Figure A.15: Raw data muons

Below the different muon M_T distributions for every cut are shown.

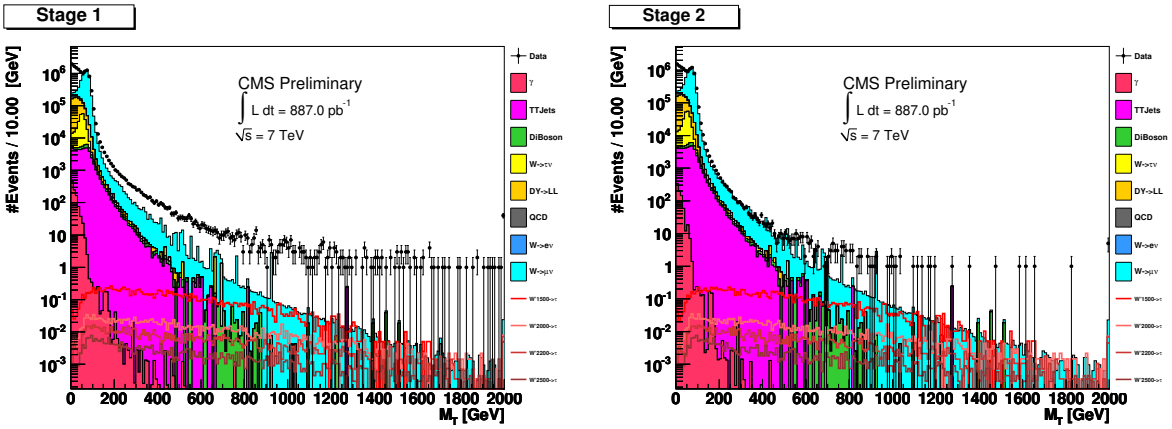

Figure A.16: Muon stages

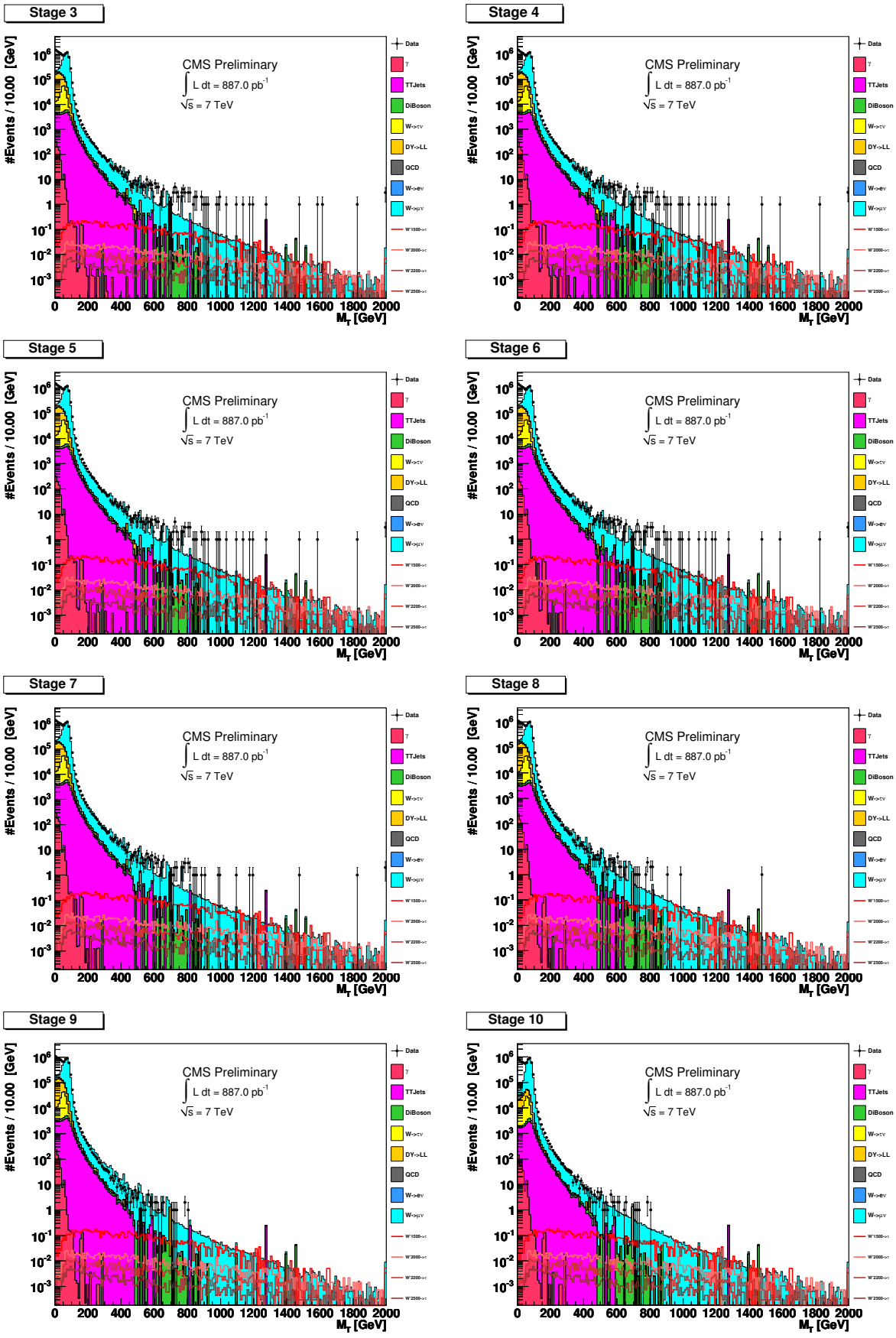

Figure A.17: Muon stages

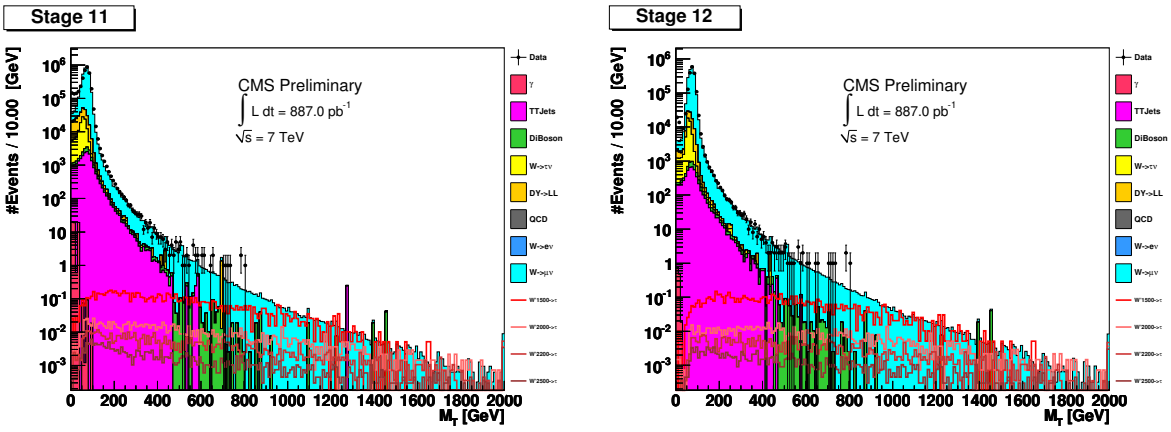

Figure A.18: Muon stages

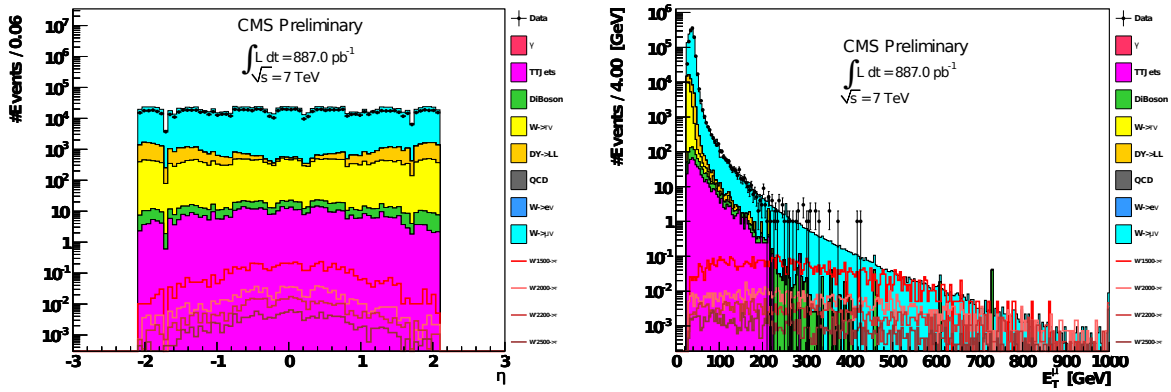

Figure A.19: Muons: η and E_T distributions

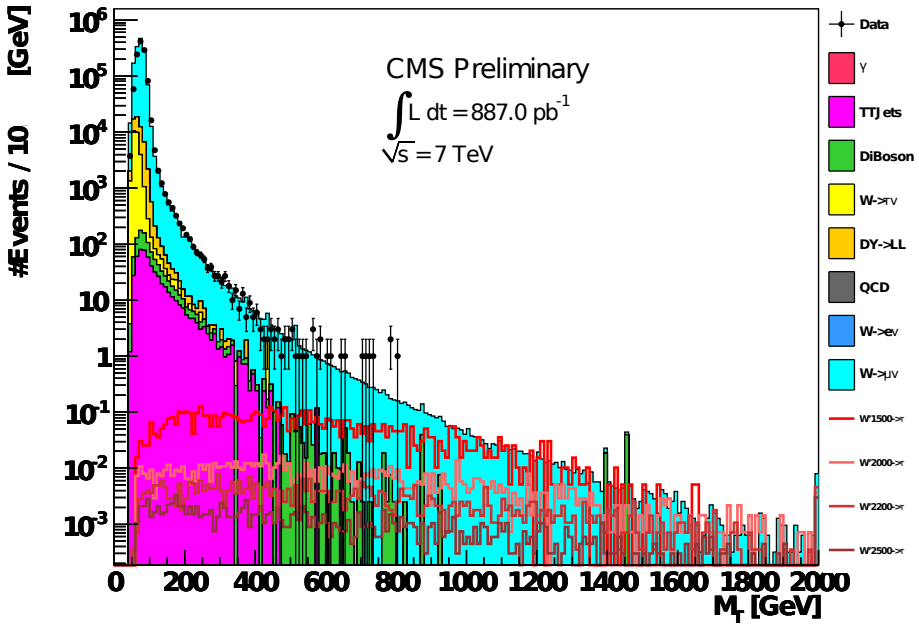

Figure A.20: Muon M_T-distribution after all quality and kinematic cuts

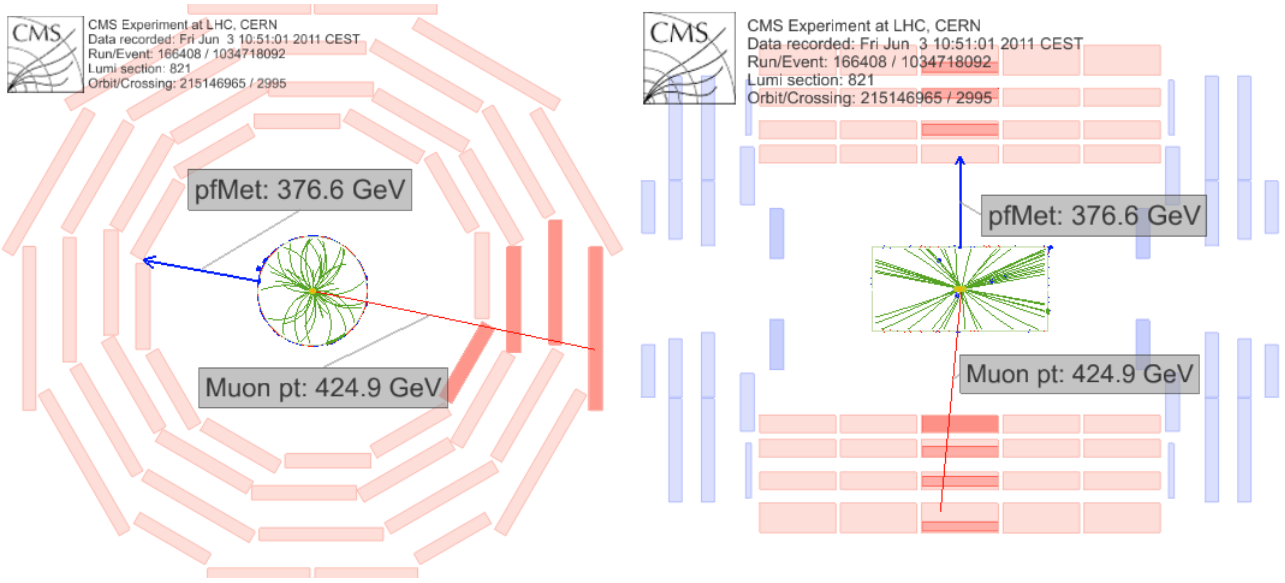

Figure A.21: Event display of the highest M_T muon event

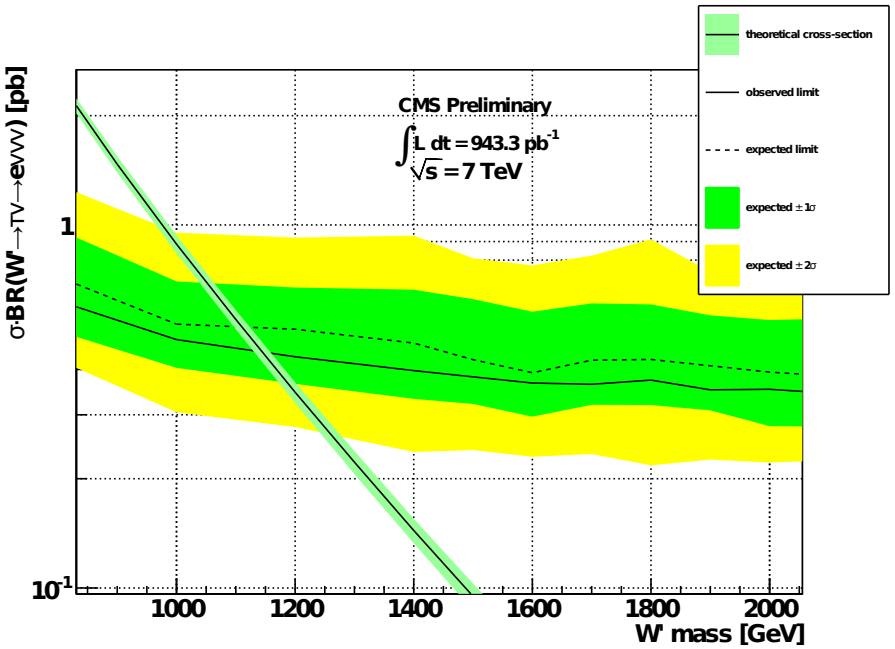

Figure A.22: Electron limit plot

quantity	value	uncertenty
luminosity [pb^{-1}]	942.8	56.6 (6%)
number of background events	230.2	3.8
number of observed events	224	-
signal efficiency [%] $m_{W'} = 1000$ GeV	6.3	0.2

Table A.5: Used values and uncertenties for the electron limit calculation.

Below the different M_T distributions for every cut are shown.

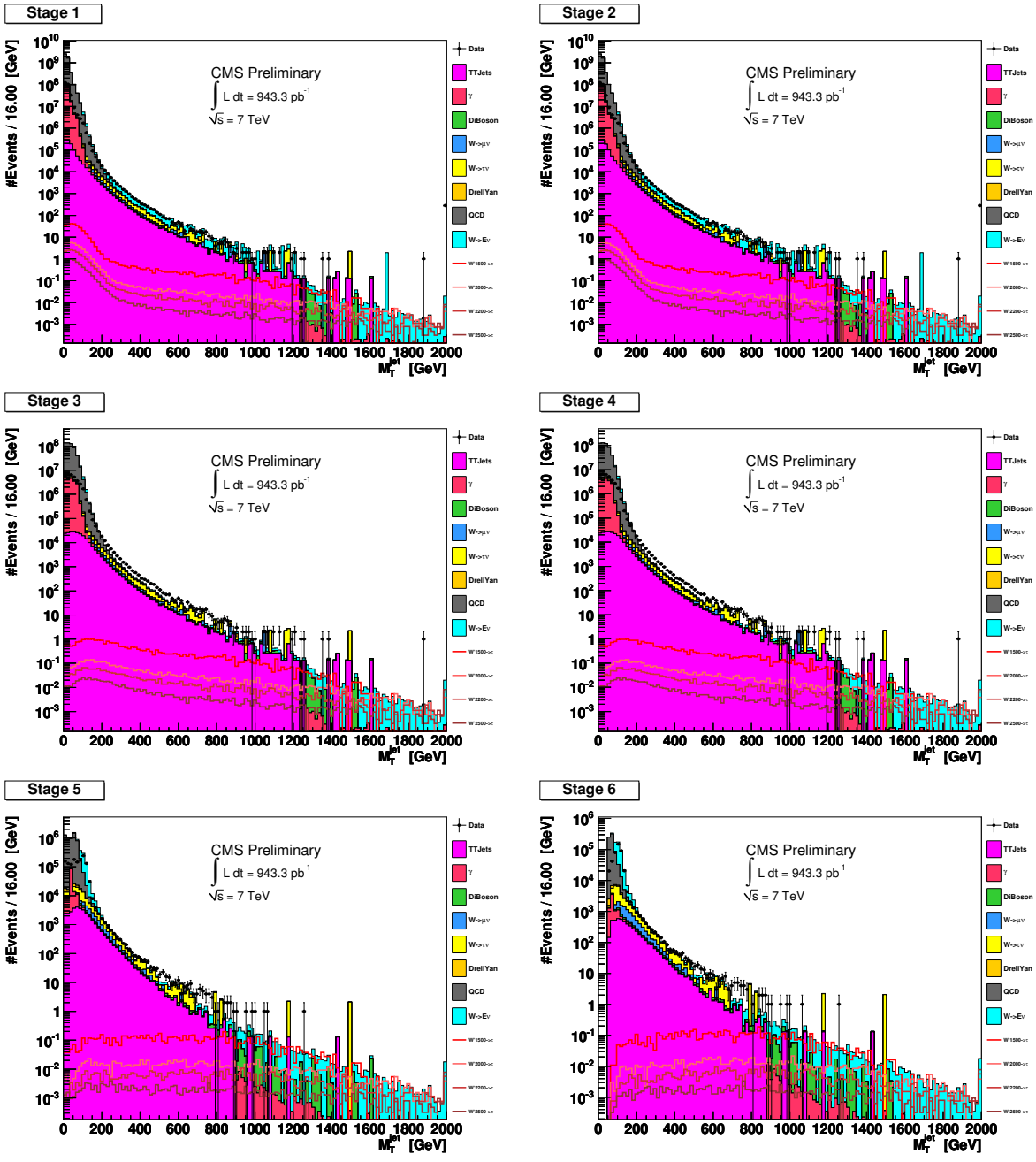

Figure A.23: Jet stages

Below the different M_T distributions for every cut are shown.

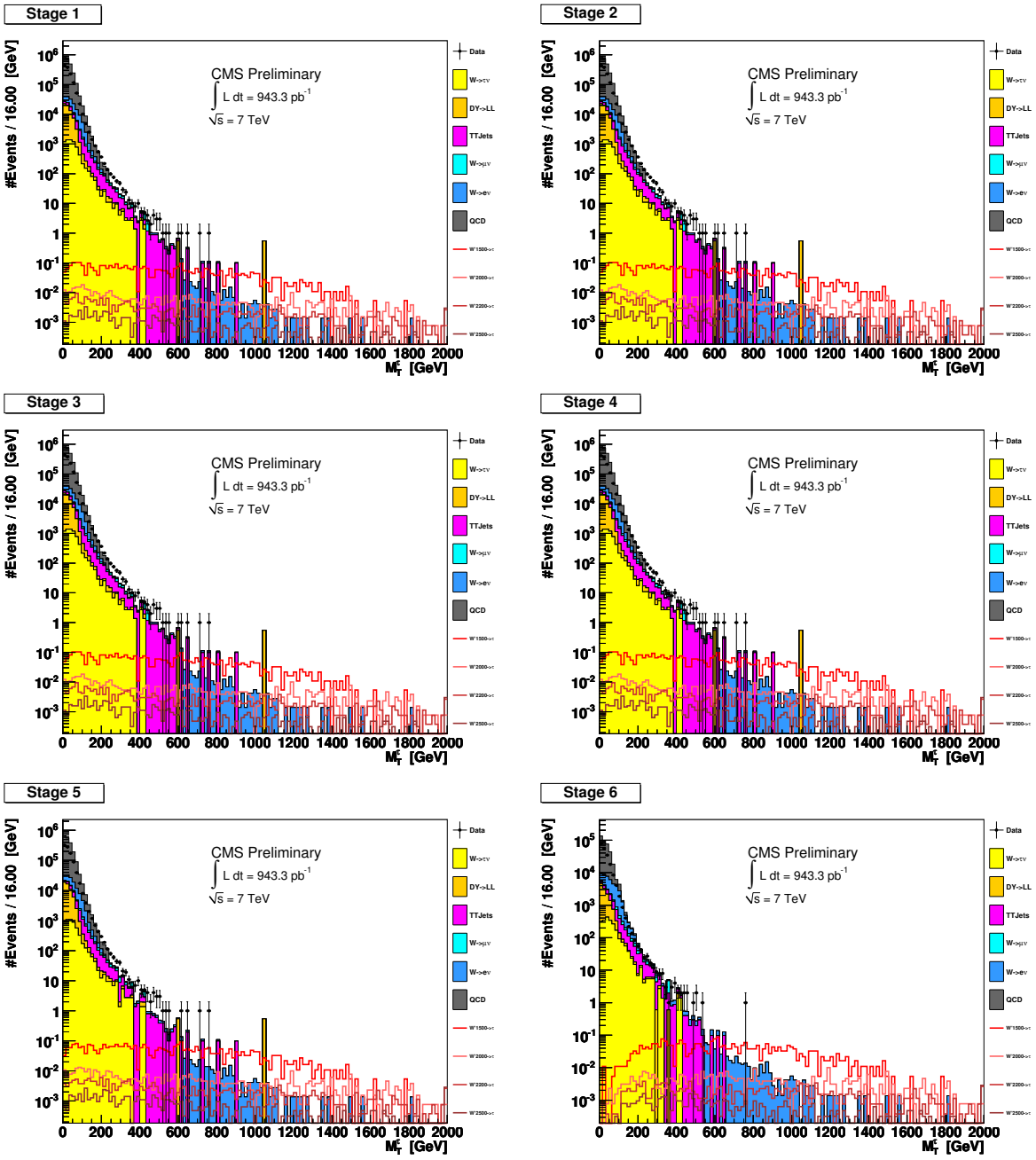

Figure A.24: Pftau stages

BIBLIOGRAPHY

[1] http://madgraph.hep.uiuc.deu/.

[2] https://twiki.cern.ch/twiki/bin/viewauth/CMS/JetID, 2009.

[3] http://en.wikipedia.org/wiki/File:Standard_Model_of_Elementary_Particles.svg, 2011.

[4] *Spring 2011 CMS MonteCarlo Production*. https://twiki.cern.ch/twiki/bin/viewauth/CMS/ProductionSpring2011, 2011.

[5] G.P.S.M. Cacciari and G. Soyez. The anti-kt jet clustering algorithm. *JHEP*, (04):063, 2008.

[6] CERN. http://cdsweb.cern.ch/record/1115614, 2008.

[7] CMS Collaboration. http://cms.web.cern.ch/cms/Media/Images/Detector/Detector%20Drawings/index.html, 2011.

[8] The CMS Collaboration. Particle-flow event reconstruction in cms and performance for jets, taus, and e_T^{miss}. *CMS PAS PFT-09/001*, 2009.

[9] The CMS Collaboration. Search for w′ in the leptonic channels in pp collisions at sqrt(s)=7 tev. *CMS PAPER EXO-11-024*, 2011.

[10] B. Dorney. http://www.quantumdiaries.org/wp-content/uploads/2011/06/JetConeWithTracks.png, 2011.

[11] A. Caldwell et al. http://www.mppmu.mpg.de/bat/, 2011.

[12] M. Bachtis et al. *Study of tau reconstruction algorithms using pp collisions data collected at* $\sqrt{s} = 7$TeV. 2010.

[13] S. Alioli et al. http://powhegbox.mib.infn.it/, 2011.

[14] T. Söstrand et al. http://home.thep.lu.se/~torbjorn/Pythia.html, 2011.

[15] S. Chatrchyan et al. (CMS Collaboration). *The CMS experiement at the CERN LHC*. 2008 JINST S08004, 2008.

[16] K Nakamura et al. (Particle Data Group). *Review of Particle Physics*. 2010.

[17] M. Ruiz-Altaba G. Altarelli, B. Mele. Searching for new heavy vector bosons in $p\bar{p}$ colliders. *Z. Phys. C - Particles and Fields*, (45):109–121, 1989.

[18] S. Schmitz G.Kukartsev, G. Schott. https://twiki.cern.ch/twiki/bin/viewauth/CMS/RooStatsCl95, 2011.

[19] HEEP Group. https://twiki.cern.ch/twiki/bin/viewauth/CMS/HEEPElectronID, 2009.

[20] A. Harel and P. Schieferdecker. Calorimeter jet quality criteria for the first cms collision data, and preparations for calibrating their efficiencies. *CMS AN-2009/087*, 2009.

[21] S. Knutzen. *Studie zur Sensitivität des CMS Experiments auf schwere, geladene Vektorbosonen mit Myonen im Endzustand*. 2010.

[22] Philip Bryant Lyndon Evans. *LHC Machine*. 2008 JINST S08001.

[23] Carsten Magass. https://twiki.cern.ch/twiki/bin/viewauth/CMS/ACSusyAnalysis, 2010.

[24] P. Millet. *Studie zur Sensitivität des CMS Experiments auf schwere, geladene Vektorbosonen mit Elektronen im Endzustand*. 2010.

[25] MuonPOG. https://twiki.cern.ch/twiki/bin/viewauth/CMS/MuonRecoPerformance2010, 2010.

[26] The ROOT Team. http://root.cern.ch/drupal/, 2011.

LIST OF FIGURES

Figure 2.1 Particles of the Standard Model [3] 3
Figure 3.1 LHC layout: Shown is the LHC ring, the experimental caverns for ATLAS, ALICE, CMS and LHCb and also the last pre-accelerator the Super Proton Synchrotron (SPS)[6]. 5
Figure 4.1 complete CMS detector: One can clearly see the positions of the different sub-detectors and also the general layout of the barrel around the beam pipe in the middle and the two endcaps [7]. 7
Figure 4.2 CMS tracker: The different detector modules are represented each by a line [15]. 8
Figure 4.3 CMS Ecal [15] 9
Figure 4.4 Hcal + Muon[15] 10

Figure 5.1 Jet: Shown are the different tracks of the measured charged particles and the jet-cone describing the jet [10]. 12

Figure 6.1 complete decay chain 15

Figure 6.2 τ decay Feynman graph 15

Figure 6.3 Kinematics of the leptonic tau decay: Here is shown the $E_T/\not{E}_T$ ratio and $\Delta\varphi$ for the final state lepton (e or μ) and the missing transverse energy calculated out of the three neutrinos. 17

Figure 6.4 Kinematics hadronic tau decay: $E_T/\not{E}_T$ ratio and $\Delta\varphi$ for the hadronic jet and missing transverse energy calculated out of the two neutrinos, as for the leptonic decaying tau we see that $\Delta\varphi$ is about π and $E_T/\not{E}_T$ is about one. The peak in the lower region of $E_T/\not{E}_T$ can be explained by pileup or underlying events. 18

Figure 6.5 E_T^{τ} vs. E_T^{lep}: As we can see that the energy of the tau is clearly defined, with a peak at 750 GeV, but the charged leptons that come from the decay of the tau do not have this clear shape anymore, this can be explained by the subsequent decay of the tau which results in a smearing of E_T due to more decay products. 19

Figure 6.6 Generator level M_T-distribution: M_T^{τ} vs. M_T^{lep}: In the left plot we see the transverse mass calculated out of the generated tau and neutrino coming directly from the W' and on the right side the transverse mass of the lepton of the tau decay and all three neutrinos is shown. 20

Figure 7.1 Raw data electrons: Shown is the M_T-distribution of the electrons, the difference between data and the Monte Carlo samples is mainly due to different triggers and also different preselection in the skimmer. 24

Figure 7.2 cut flow electron for quality + kinematic cuts 26

Figure 7.3 cut flow muon quality and kinematic cuts 27

Figure 7.4 Electron lower $E_T/\not{E}_T$ cut 28

Figure 7.5 Electron $\Delta\varphi$ cut 29

Figure 7.6 Resulting data electrons: One can clearly see the Standard Model W peak in the low M_T region. The signal is evenly distributed as expected from the generator level analysis (comp. 6.6) and has no characteristic peak. For comparison the final M_T-distribution of a $W' \to e\nu$ sample (green in the plot) with a mass of 1500 GeV with its characteristic Jacobean Peak is shown. 31

Figure 7.7 Resulting data muons: As in the electron distribution we can see the Standard Model W peak in the low M_T region and signal is evenly distributed with no characteristic peak an event display of the highest M_T event can be seen in the appendix (see section A.5). As a comparison the final M_T-distribution of a $W' \to \mu\nu$ sample with a mass of 1500 GeV is shown, like for the electrons we see the jacobean peak and the over all bigger signal, because of the higher branching ratio, the difference to the electron channel can be explained by the lower p_T resolution for high p_T-muons. 32

Figure 7.8 Muon limit plot: We can see that the observed cross-section confirms the expected one, and we get an W' mass limit of $m_{W'} > 1075$ GeV. 33

Figure 7.9 Combined limit plot: By combining the limits of the electron and muon we get a mass limit of $m_{W'} > 1150$ GeV from the intersection of observed cross-section and the theoretical one with 'Reference Model' branching ratios. If we assume that the W' decays leptonically only in taus we get a mass limit of $m_{W'} > 1500$ GeV from the intersection of observed and theoretical cross-section with only τ branching ratio. 34

Figure 8.1 Jet raw data: The difference between data and background Monte Carlo samples can be explained by the different triggers used for the skimming of the data and background samples. 39

Figure 8.2 Particle-flow tau raw data: The same difference between data and Monte Carlo samples as for the jets can be seen, and is expected, because the particle-flow taus are reconstructed out of jets. 40

Figure 8.3 Jet cutflow 41

Figure 8.4 Particle-flow tau cutflow 42

Figure 8.5 Upper $E_T/\not{E}_T$ cut jets: We can see a shift of the bump to an $E_T/\not{E}_T$ ratio slightly higher than 1, because of lower missing transverse energy in this events. 43

Figure 8.6 Resulting jet data: As in the leptonic decays of the tau, we can clearly see the Standard Model W peak, but no characteristic peak in the signal distribution. 44

Figure 8.7 Resulting particle-flow tau data: The distribution looks very similar to the one for the hadronic jets, with two major differences, first that we have only 1/10 of the data because many events contain jets but much less are tau-like. Second because the signal is quite similar to the hadronic jets a much higher signal to background ratio in the high M_T region. 45

Figure 8.8 Hadronic limit plot: We can see that the observed limit for the hadronic jets has no intersection with the theoretical cross-section, and can only guess that it is around 600 GeV, because we had no samples with a so low W' mass. Contrary to that we can get a clear mass limit of $m_{W'} > 1000$ GeV for the particle-flow taus. 46

Figure 8.9 Measured distance the tau flew from the interaction point to its decay point. 47

Figure 8.10 Measured hadronic decay modes of the tau (explanation for the x-axis: the number of charged and neutral particles are listed e.g 3c + 2n means there were three charged and two neutral particles reconstructed). 48

Figure A.1 E_T^{τ} vs. E_T^{jet}: Transverse energy distribution for the tau coming from the W' and the jet coming from the tau. 53

Figure A.2 $E_T^{\nu_\tau}$ vs. $\not{E}_T$: Transverse energy of the neutrino coming from the W' decay and the missing transverse energy calculated out of the three neutrinos in a leptonic decaying tau. 54

Figure A.3 M_T^{τ} vs. M_T^{jets}: Transverse mass of the tau and neutrino from the W′ decay and transverse mass calculated out of the hadronic jet coming from the tau decay and the two neutrinos in the event as missing transverse energy. 54
Figure A.4 Electron $E_T/\not{E}_T$ cut 55
Figure A.5 Electron $\Delta\varphi$ cut 56
Figure A.6 Muon upper $E_T/\not{E}_T$ cut 56
Figure A.7 Muon lower $E_T/\not{E}_T$ cut 57
Figure A.8 Muon $\Delta\varphi$ cut 57
Figure A.9 Jet lower $E_T/\not{E}_T$ cut 58
Figure A.10 Jet upper $E_T/\not{E}_T$ cut 58
Figure A.11 Jet $\Delta\varphi$ cut 59
Figure A.12 Electron stages 63
Figure A.13 Electrons: η and E_T distributions 65
Figure A.14 Electron M_T-distribution after all quality and kinematic cuts 65
Figure A.15 Raw data muons 66
Figure A.16 Muon stages 66
Figure A.17 Muon stages 67
Figure A.18 Muon stages 68
Figure A.19 Muons: η and E_T distributions 68
Figure A.20 Muon M_T-distribution after all quality and kinematic cuts 69
Figure A.21 Event display of the highest M_T muon event 69
Figure A.22 Electron limit plot 70
Figure A.23 Jet stages 71
Figure A.24 Pftau stages 72

LIST OF TABLES

Table 6.1 τ decay modes and branching ratios [16] 16
Table 7.1 electron background samples 22
Table 7.2 muon background samples 23
Table 7.3 signal samples 23
Table 7.4 used data sets 23
Table 7.5 Used values and uncertenties for the muon limit calculation. 34
Table 7.6 Efficiencies of leptonic decaying taus: The event numbers and ratios are calculated from the listed W′ samples and are not scaled. 35

Table 8.1 Background samples for hadronic jets and particle-flow taus 38
Table 8.2 Signal samples 38
Table 8.3 Comparison between measured and theoretical hadronic decay modes relative to all decay modes. 49
Table 8.4 Particle-flow tau efficiency 49
Table A.1 Monte Carlo samples electron channel 60
Table A.2 Monte Carlo sample muon channel 61
Table A.3 Signal samples 61
Table A.4 All used triggers 62
Table A.5 Used values and uncertenties for the electron limit calculation. 70

A.9 ACKNOWLEDGMENTS

Here I want to thank the people who made this thesis possible.

First I want to thank Prof. Dr. Hebbeker for making this highly interesting thesis, on the latest high-energy physics research, possible.

Second I want to thank the Aachen CMS IIIA group for the good working atmosphere and the help for every problem. Especially I want to thank the other members of the Aachen W′ group: Dr. Kerstin Hoepfner, Kay J. Krause, Jan-Frederik Schulte and Sebastian Thuer for the excellent support and the proof reading of this thesis. Dr. Hoepfner I want to thank for the excellent help, support and advise throughout the whole work on this thesis.

Last but not least I want to thank Franziska Ludwicki for the advice on the thesis and the language.

DECLARATION

Hiermit versichere ich, Sören Erdweg, dass ich die Arbeit selbstständig verfasst und keine anderen als die angegebenen Quellen und Hilfsmittel benutzt, sowie Zitate kenntlich gemacht habe.

Erkelenz, den 25.07.2011